Probe Of Extreme Multi-Messenger Astrophysics

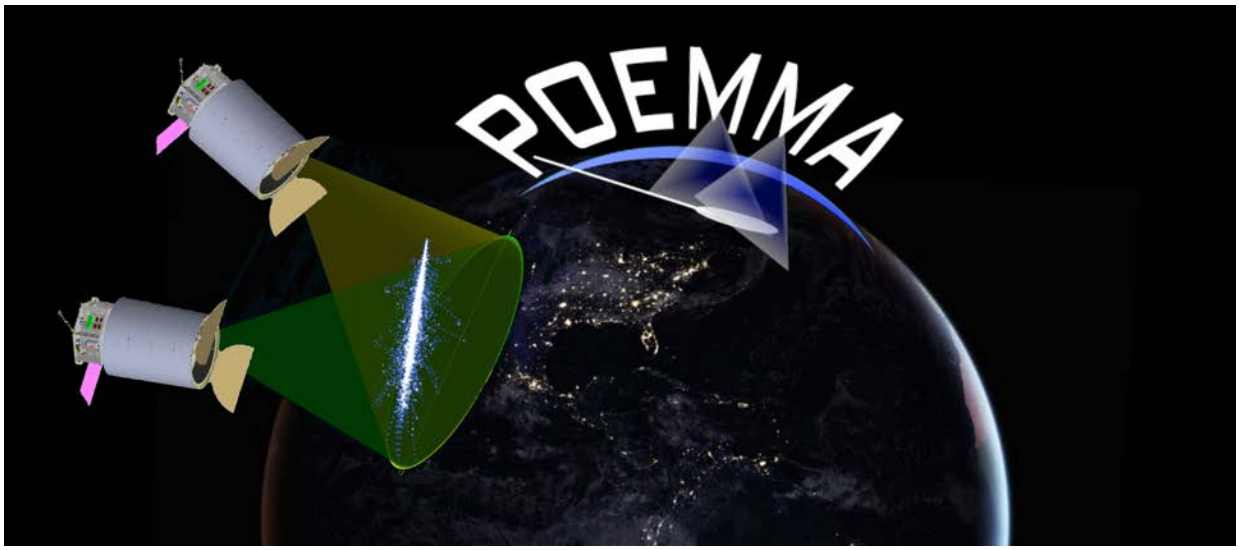

POEMMA: Probe of Extreme Multi-Messenger Astrophysics

A V. Olinto,[1] J. H. Adams,[2] R. Aloisio,[3] L. A. Anchordoqui,[4] D. R. Bergman,[5] M. E. Bertaina,[6] P. Bertone,[7] F. Bisconti,[8] M. Casolino,[9] M. J. Christl,[7] A. L. Cummings,[3] I. De Mitri,[3] R. Diesing,[1] J. Eser,[10] F. Fenu,[6] C. Guepin,[11] E. A. Hays,[12] E. G. Judd,[13] J. Krizmanic,[12] E. Kuznetsov,[2] S. Mackovjak,[14] J. McEnery,[12] J. W. Mitchell,[12] A. Neronov,[15] F. Oikonomou,[16] A. N. Otte,[17] E. Parizot,[18] T. Paul,[4] J. S. Perkins,[12] G. Prévôt,[18] P. Reardon,[2] M. H. Reno,[19] M. Ricci,[20] F. Sarazin,[10] K. Shinozaki,[6] J. F. Soriano,[4] F. Stecker,[12] Y. Takizawa,[9] M. Unger,[21] T. Venters,[12] L. Wiencke,[10] and R. M. Young[7]

[1]*The University of Chicago, Chicago, IL, USA*
[2]*University of Alabama, Huntsville, AL, USA*
[3]*Gran Sasso Science Institute, L'Aquila, Italy*
[4]*City University of New York, Lehman College, NY, USA*
[5]*University of Utah, Salt Lake City, Utah, USA*
[6]*Universita' di Torino, Torino, Italy*
[7]*NASA Marshall Space Flight Center, Huntsville, AL, USA*
[8]*INFN, Section of Turin, Turin, Italy*
[9]*RIKEN, Wako, Japan*
[10]*Colorado School of Mines, Golden, CO, USA*
[11]*Sorbonne Universités, Institut dAstrophysique de Paris, Paris, France*
[12]*NASA Goddard Space Flight Center, Greenbelt, MD, USA*
[13]*Space Sciences Laboratory, University of California, Berkeley, CA, USA*
[14]*Institute of Experimental Physics, Slovak Academy of Sciences, Kosice, Slovakia*
[15]*University of Geneva, Geneva, Switzerland*
[16]*European Southern Observatory, Garching bei München, Germany*
[17]*Georgia Institute of Technology, Atlanta, GA, USA*
[18]*APC, Univ Paris Diderot, CNRS/IN2P3, CEA/Irfu, Obs de Paris, Sorbonne Paris Cité, France*
[19]*University of Iowa, Iowa City, IA, USA*
[20]*Istituto Nazionale di Fisica Nucleare - Laboratori Nazionali di Frascati, Frascati, Italy*
[21]*Karlsruhe Institute of Technology, Karlsruhe, Germany*

Contents

I. POEMMA OVERVIEW

The Probe Of Extreme Multi-Messenger Astrophysics (POEMMA) is a probe Class B mission designed to observe ultra-high energy cosmic rays (UHECRs) and cosmic neutrinos from space. POEMMA will monitor colossal volumes of the Earth's atmosphere to detect extensive air showers (EASs) produced by extremely energetic cosmic messengers: UHECRs above 20 EeV and cosmic neutrinos above 20 PeV over the entire sky.

POEMMA is comprised of two identical observatories flying in formation to detect EASs in mono and stereo modes. Each observatory is composed of a 4-meter photometer designed with Schmidt wide (45°) field-of-view (FoV) optics (see Figure 1) and a spacecraft bus. The photometer focal surface has a hybrid design for two complementary capabilities: a fast (1 μs) ultraviolet camera to observe fluorescence signals and an ultra-fast (10 ns) optical camera to detect Cherenkov signals. EASs from UHECRs and cosmic neutrinos are observed from an orbit altitude of 525 km and a range of attitudes in the dark sky. POEMMA will point from close to the nadir, to optimize stereo fluorescence observations, to about 47° from the nadir to monitor the Earth's limb (located at 67.5°) for Cherenkov emission from EASs from cosmic neutrinos (below the limb) and UHECRs ($\sim 2°$ above the limb).

POEMMA will provide a significant increase in the statistics of observed UHECRs at the highest energies over the entire sky and will have a target of opportunity (ToO) follow-up program for cosmic neutrinos from extremely energetic transient astrophysical events.

POEMMA will:

• **Discover the nature and origin of the highest-energy particles in the universe.** Where do UHECRs come from? What are these extreme cosmic accelerators and how do they accelerate to such high energies? What is the UHECR composition at the highest energies? What are the magnetic fields in the galactic and extragalactic media? How do UHECRs interact in the source, in galactic and extragalactic space, and in the atmosphere of the Earth?

• **Discover neutrino emission above 20 PeV for extreme astrophysical transients.** What is the high-energy neutrino emission of gravitational wave events? Do binaries with black holes, white dwarfs, and neutron stars produce high-energy neutrinos when they coalesce? Neutrino observations will elucidate the underlying dynamics of blazar flares, gravitational wave events, gamma-ray bursts, newborn pulsars, tidal disruption events, and other transient events as seen by neutrinos?

• **Probe particle interactions at extreme energies.** POEMMA can test models with physics beyond the Standard Model (BSM) through cosmic neutrino observations from hundreds of PeVs to tens of ZeVs;

• **Observe Transient Luminous Events** and study the dynamics of the Earth's atmosphere, including extreme storms;

• **Observe Meteors**, thereby contributing to the understanding of the dynamics of meteors in the Solar System;

• **Search for Exotic particles** such as nuclearites.

POEMMA will provide new **Multi-Messenger Windows** onto the most energetic environments and events in the universe, enabling the study of new astrophysics and particle physics at these otherwise inaccessible energies.

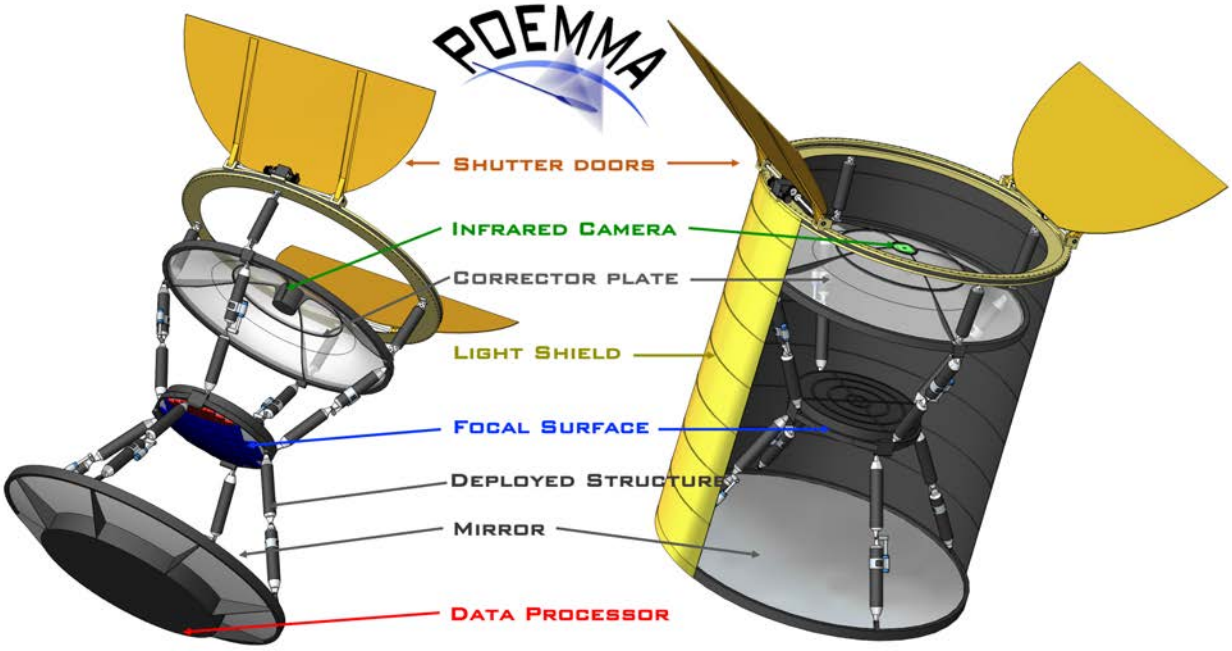

FIG. 1: Concept of the POEMMA photometer with major components identified.

TABLE I: POEMMA Specifications:

Photometer	Components		Spacecraft	
Optics	Schmidt	45° full FoV	Slew rate	90° in 8 min
	Primary Mirror	4 m diam.	Pointing Res.	0.1°
	Corrector Lens	3.3 m diam.	Pointing Know.	0.01°
	Focal Surface	1.6 m diam.	Clock synch.	10 ns
	Pixel Size	3×3 mm^2	Data Storage	7 days
	Pixel FoV	0.084°	Communication	S-band
PFC	MAPMT (1μs)	126,720 pixels	Wet Mass	3,450 kg
PCC	SiPM (20 ns)	15,360 pixels	Power (w/cont)	550 W
Photometer	(One)		Mission	(2 Observatories)
	Mass	1,550 kg	Lifetime	3 year (5 year goal)
	Power (w/cont)	700 W	Orbit	525 km, 28.5° Inc
	Data	< 1 GB/day	Orbit Period	95 min
			Observatory Sep.	~25 - 1000 km

Each Observatory = Photometer + Spacecraft; POEMMA Mission = 2 Observatories

II. POEMMA EXTREME MULTI-MESSENGER SCIENCE

A. Introduction

The main scientific goals of POEMMA are to discover the elusive sources of UHECRs, cosmic rays with energies above 10^{18} eV ($\equiv 1$ EeV), and to observe cosmic neutrinos from multi-messenger transients. POEMMA exploits the tremendous gains in both UHECR and cosmic neutrino exposures offered by space-based measurements, *including full-sky coverage of the celestial sphere*. For cosmic rays with energies $E \gtrsim 20$ EeV, POEMMA will enable charged-particle astronomy by obtaining definitive measurements of the UHECR spectrum, composition, and source location. For multi-messenger transients, POEMMA will follow ToOs to detect the first cosmic neutrino emission with energies $E_\nu \gtrsim 20$ PeV from transients. POEMMA also has sensitivity to neutrinos with energies above 20 EeV through fluorescence observations of neutrino induced EASs. Supplementary science capabilities of POEMMA include probes of physics beyond the Standard Model of particle physics, the study of atmospheric transient luminous events (TLEs), and the search for meteors and nuclearites.

These groundbreaking measurements are obtained by operating POEMMA's two observatories (described in Figure 1 and Table I) in different orientation modes: a quasi-nadir stereo fluorescence configuration for UHECR observations and a tilted, Earth-limb viewing Cherenkov configuration for ToO neutrino searches (see Figure 2). In limb observing mode, POEMMA can simultaneously search for neutrinos and UHECRs with Cherenkov observations, while observing UHECRs with fluorescence, thanks to the POEMMA hybrid camera design.

In stereo fluorescence mode, the two wide-angle (45°) Schmidt photometers with several square meters of effective photon collecting area view a common, immense atmospheric volume corresponding to approximately 10^4 gigatons of atmosphere. The stereo mode yields one order of magnitude increase in yearly UHECR exposure compared to that obtainable by ground observatory arrays and two orders of magnitude compared to ground fluorescence observations. In the Cherenkov limb-viewing mode, POEMMA searches for optical Cherenkov signals of upward-moving EASs generated by τ-lepton decays produced by ν_τ interactions in the Earth. The terrestrial neutrino target monitored by POEMMA reaches nearly 10^{10} gigatons. In the Cherenkov mode an even more extensive volume of the atmosphere is monitored for UHECR fluorescence measurements. Thus, **POEMMA uses the Earth and its atmosphere as a gargantuan high-energy physics detector and astrophysics observatory.**

B. UHECR Science

Over a half-century since John Linsley reported the observation of a 10^{20} eV (= 100 EeV) EAS [1], the astrophysical sources of these extremely energetic cosmic rays remain unknown. UHECRs with energies ≥ 100 EeV have energies over 7 orders of magnitude higher than what terrestrial accelerators can currently achieve. A succession of increasingly large ground-based experiments (Fly's Eye [2], AGASA [3], and HiRes [4]) has led to the two leading observatories currently in operation: the Pierre Auger Observatory [5, 6] in the southern hemisphere, with $\sim 65,000$ km^2 sr yr exposure in 13 years of operation [7], and the Telescope Array (TA) [8, 9] in the northern hemisphere, with $\sim 20,000$ km^2 sr yr ex-

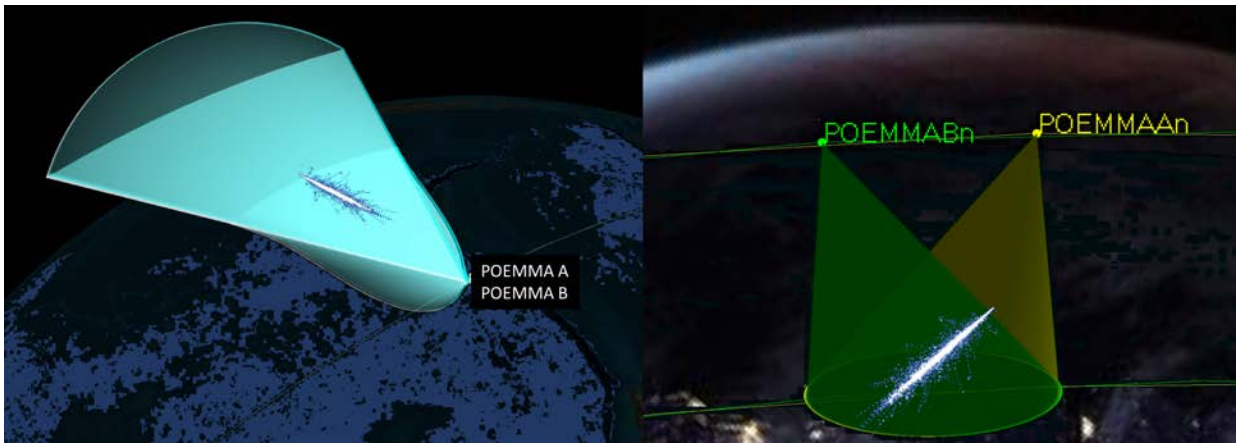

FIG. 2: POEMMA observing modes. Left: Cherenkov mode from above (UHECRs) and below (cosmic neutrinos) the limb of the Earth; Right: Stereo fluorescence mode around the nadir.

posure in 10 years (see Figure 3). POEMMA can reach between ~ $2X10^5$ to $2X10^6$ km^2 sr yr exposure in a 5 year mission.

The nature of the astrophysical sources of UHECRs and their acceleration mechanism(s) remains a mystery [10–12]. Extremely fast-spinning young pulsars [13–15], active galactic nuclei (AGN) [16–18], starburst galaxies (SBGs) [19, 20], and gamma-ray bursts (GRBs) [21, 22] can partially accommodate current Auger and TA observations, but the scarcity of observed events above tens of EeV has hindered the identification of the sources.

Both the Auger and TA observatories are giant ground-arrays of particle detectors (3,000 km^2 for Auger and 700 km^2 for TA) overseen by fluorescence telescopes (4 telescope sites for Auger and 3 for TA). These detectors observe EASs via the shower particles that hit the ground array detectors at any time of the day and, ~ 10 % of the time (in dark moonless nights), they observe the faint ultraviolet (UV) emission of atmospheric nitrogen fluorescence excited by EAS particles. Auger plans to continue observations over the next decade with enhanced detector units for the ground array, an upgrade named AugerPrime [23]. TA is now being upgraded to TAx4: an expansion of its ground-array four-fold to reach the Auger ground-array scale [24].

Figure 4 left shows an example of an EAS with a schematic development of the number of charged particles with atmospheric depth (X in g/cm^2). The EAS particles excite atmospheric nitrogen that fluoresce in the UV isotropically. The fluorescence signal of extremely energetic EASs can be observed megameters away from the shower axis. In the forward direction of the EAS development, beamed Cherenkov photons are also emitted. Figure 4 right shows the relative intensity of the UV lines in the air nitrogen fluorescence spectrum. POEMMA is designed to observe both the fluorescence UV emission and the Cherenkov emission of EASs.

Auger and TA have measured key features of UHECRs: their spectrum (up to ~ 100 EeV, see Figure 5), their composition (up to ~ 50 EeV, see Figure 6), and the sky distribution of their arrival directions. The spectrum (Figure 5 left) shows an *ankle* ~ 5 EeV and a suppression of the UHECR flux above ~ 40 EeV [25–28]. The suppression is consistent with the predicted Greisen-Zatsepin-Kuzmin (GZK) effect [29, 30] caused by energy losses of UHECRs on the cosmic microwave background as they travel astronomical distances from extragalactic sources to Earth. The same spectral feature may be produced by

the maximum energy of the sources in models that also predict a change to heavier composition at the highest energies [31].

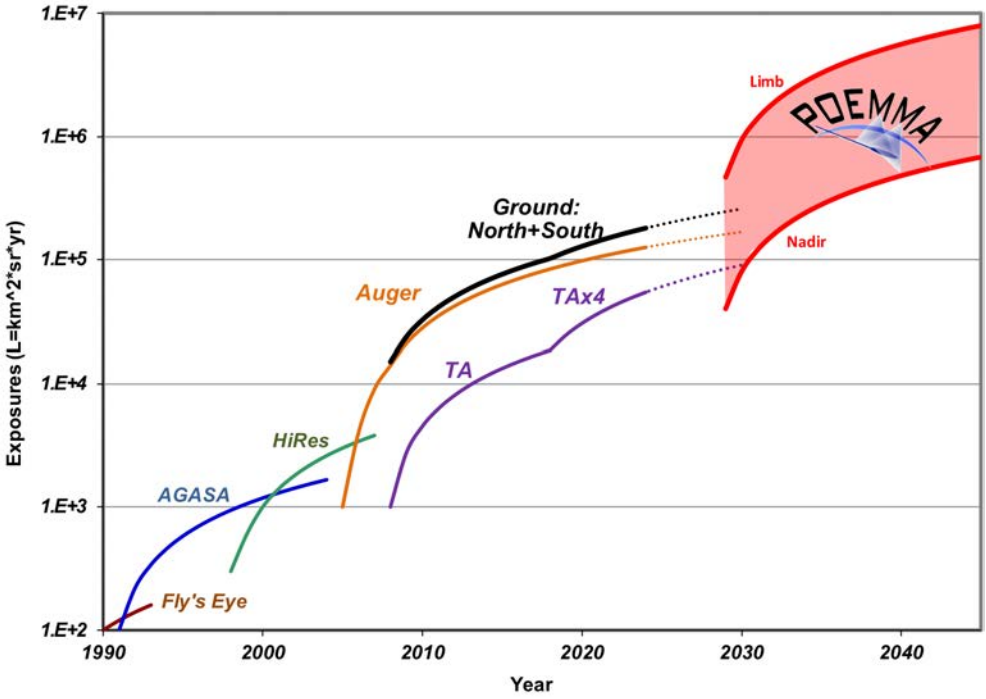

FIG. 3: The range of POEMMA's exposure growth in time as compared to current ground-based UHECR experiments depending on observation mode: from nadir to limb observations. **Dotted** lines extrapolate Auger and TAx4 observations to 2030.

In addition to spectral and composition measurements, a crucial step in unveiling the origin of UHECRs is the localization of sources in the sky distribution of their arrival directions. Since UHECRs are charged and magnetic fields fill the galactic and extragalactic media, pointing to sources is best achieved at the highest energies (or rigidities). The typical deflection of a UHECR of energy E and charge Z (in units of proton charge) in an extragalactic magnetic field $B \sim 1$ nG [32] is $\delta\theta \approx 1.5^\circ\, Z\,(10\ \mathrm{EeV}/E)$, for a source at 4 Mpc and a magnetic field coherence length of about 100 kpc [33, 34]. The deflections when crossing the Galaxy can be somewhat larger [35] $\delta\theta \sim 1^\circ\, Z\,(100\ \mathrm{EeV}/E)$, depending on the UHECR arrival trajectory through the Galaxy. These deflections suggest that large statistics of events above tens of EeV are necessary to observe small-scale anisotropies around source positions in the sky.

To date the only high-significance departure from an isotropic sky distribution of UHECRs is a dipole anisotropy reported by the Auger collaboration above 8 EeV with an amplitude $A = (6.5^{+1.3}_{-0.9})\%$ pointing in the direction $(l, b) = (233^\circ, -13^\circ) \pm 10^\circ$ in galactic coordinates [36]. This important milestone confirms the expectation that the sources of UHECRs are extragalactic, as the dipole shows no correlation with the galactic plane. Hints of clustering in the sky distribution have been reported for energies above ~ 40 to 60 EeV: TA reports a hotspot in its sky distribution [37, 38] and Auger finds a significant correlation with SBGs and a weaker association with gamma-ray emitting active galactic nuclei (γAGN) [39]. These hints can reach 5σ significance with a dramatic increase in

exposure above 60 EeV [40, 41]. POEMMA will collect a dataset larger than the current statistics of Auger and TA combined (see Figure 3). Thus, POEMMA will turn the TA and Auger anisotropy hints (and/or other anisotropy signals yet to be discovered) into significant detections to finally discover the locations of the UHECRs sources.

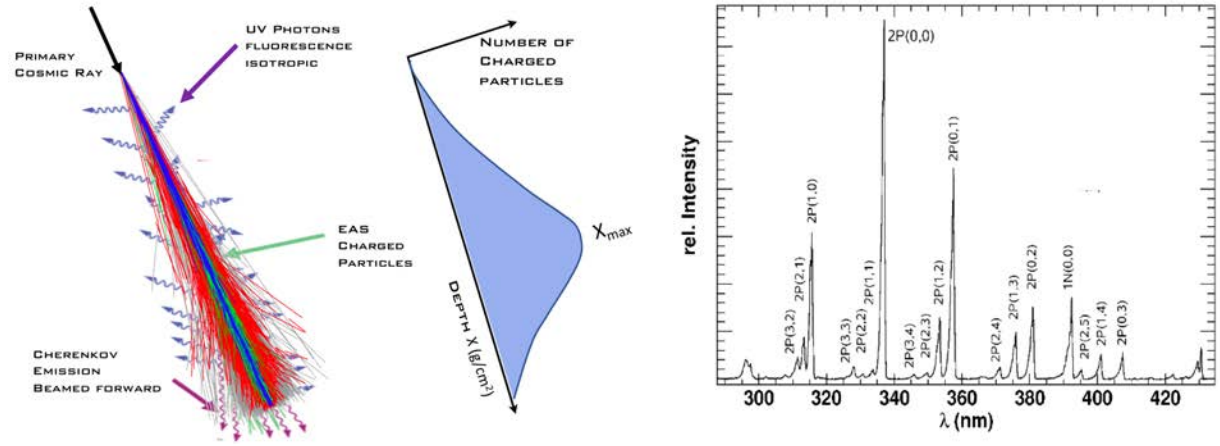

FIG. 4: Left: Extensive Air-Shower development simulation with a schematic of the number of charged particles as a function of depth and shower maximum indicated by $X_{\max}$ [42, 43]. Right: Measurement of the nitrogen fluorescence spectrum of dry air showing relative intensity of lines in the UV range [45].

C. POEMMA UHECR Performance

POEMMA addresses the challenges of discovering the sources of UHECRs by the dramatic increase in exposure enabled by space-based platforms. Figure 3 shows the POEMMA mission exposure range from pointing at the nadir to limb observations compared to extrapolations of the current ground-based experiments. POEMMA stereo nadir mode (Figure 2 right) enables excellent angular, energy, and composition resolution, while the limb observing mode (Figure 2 left) gives unparalleled volumes of monitored atmosphere for orders of magnitude increase in the statistics of observed UHECRs.

POEMMA is designed to obtain definitive measurements of the UHECR spectrum, composition, and source locations for $E \gtrsim 20$ EeV. EAS fluorescence signals are observed as video recordings with 1μs snapshots. Each observatory records an EAS trace in its focal surface (see Figure 20 right), which defines an observer-EAS plane. In stereo mode, the intersection of the two observer-EAS planes defines the geometry of the EAS trajectory. Precise reconstruction of the EAS is achieved for opening angles between these two planes larger than $\sim 5^\circ$. In mono observations, the distance to the EAS in the observer-EAS plane is determined by the evolution in time of the EAS and a model of the atmosphere.

Detailed simulations of POEMMA's UHECR exposure, angular resolution, and composition ($X_{\max}$) resolution were performed using POEMMA's instrument design. Figure 7 shows POEMMA's stereo reconstructed angular resolution, which is $\lesssim 1.5^\circ$ above 30 EeV. The stereo trigger condition in each satellite leads to a highly efficient reconstruction fraction of $\sim 80\%$, with losses due mainly to the requirement of the $\sim 5^\circ$ opening angle

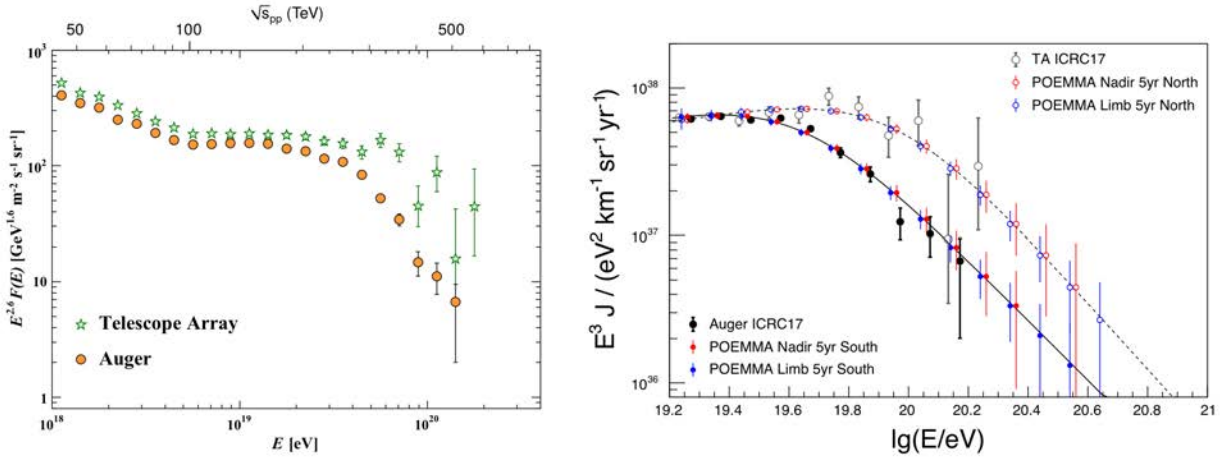

FIG. 5: Left: UHECR spectrum as measured by Auger (orange) and TA (green) [41, 44]. Right: Simulated POEMMA spectra extrapolating either the Auger spectrum (black dots and solid line) or the TA spectrum (black open circles and dotted line) for both nadir (red) and limb (blue) observations, shown for energies above $10^{19.2}$ eV.

between each EAS geometrical plane. The fine angular resolution leads to accurate 3-dimensional EAS reconstruction with energy resolution of ~ 20% and $X_{\rm max}$ resolution of ~ 30 g/cm^2 above ~ 50 EeV improving to ~ 20 g/cm^2 above ~ 100 EeV.

The UHECR energy threshold is set by the brightness of the EASs with respect to the dark-sky airglow background in the EAS fluorescence band of $300 < \lambda/\text{nm} < 500$ at the POEMMA focal surface. The near UV filter over the MAPMTs in the POEMMA Fluorescence Camera combined with the ~ 6 m^2 optical aperture of each POEMMA instrument yields an UHECR energy threshold of ~ 20 EeV.

POEMMA's UHECR exposure leads to the precise measurement of the spectrum at energies higher than reached by current observatories. Figure 5 right shows simulated POEMMA spectra extrapolating the Auger spectrum to higher energies in filled circles following the solid line. If the extrapolation is based on the TA spectrum (black open circles and dotted line), the POEMMA measurement will reach higher energies for both nadir (red) and limb (blue) observations. The impact of the POEMMA exposure in the spectrum is clear for energies above ~ 100 EeV, where new spectral features can signal source signatures such as the effect of the closest sources in a given hemisphere [10–12].

POEMMA observations allows the study of different composition models at highest energies, where composition should simplify due to propagation effects (see, e.g., [10]). The $X_{\rm max}$ resolution of POEMMA can decompose EASs into four nuclear elements, gamma-rays, and neutrinos in the highest energy range [46]. Auger observations show an interesting evolution of the composition with energy consistent with the maximum energy models [7]. The current paucity of UHECR data above 40 EeV (see Figures 6 and 8 right) strongly limits the ability to definitively test different source models with the spectral behavior and composition trends. Figure 6 shows the ability of POEMMA to extend composition measurements through the observation of the EAS maximum, X_{max}, and the fluctuations about the mean of the maximum, σ_{max}, for energies well past leading observations by Auger. In addition, if *hot-spots* in the sky are observed with more than 20 events, POEMMA can study a given source composition by the evolution of the *hot-spot*

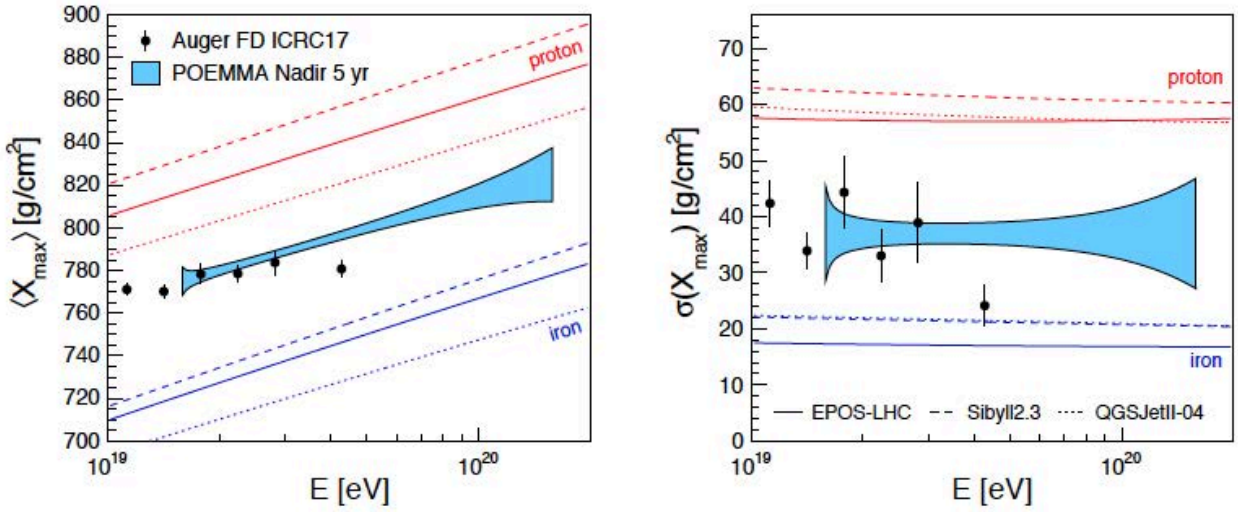

FIG. 6: Capability of POEMMA to measure $\langle X_{\rm max}\rangle$ and $\sigma(X_{\rm max})$ for composition studies at UHE. The width of the blue band illustrates the expected statistical uncertainties given the number of events per 0.1 in logarithm of energy in five year nadir operation, the $X_{\rm max}$ resolution and efficiency for $\theta < 70°$ and intrinsic shower-to-shower fluctuations of 40 g/cm^2. The band spans the energy range for which more than 10 events are within a 0.1 dex bin (assuming the Auger spectrum). The black dots are fluorescence data from Auger ICRC 2017 [7].

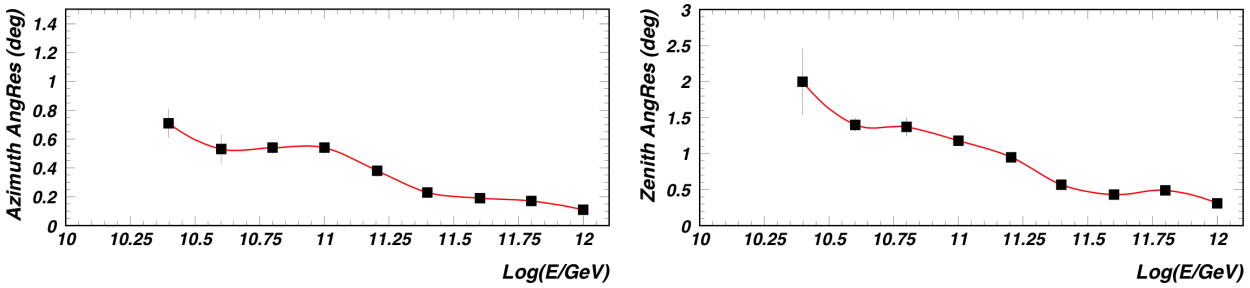

FIG. 7: POEMMA's stereo-reconstructed angular resolution versus UHECR energy: azimuth (left) zenith (right).

shape with energy [47].

POEMMA is equally sensitive to UHECR sources in both the northern and southern hemisphere. POEMMA has full-sky coverage due to its orbit at 525 km altitude and 28.5° inclination and the very large FoV (45°) for each observatory. Figure 8 left shows the differential exposure as a function of declination for five years of POEMMA operations in nadir mode (purple lines) and limb mode (red lines) observations. The exposures of Auger and TA (including the TAx4 upgrade) are shown as black (TA) and green (Auger) lines respectively assuming operations until 2030.

The nadir observation coverage is shown for two EASs energies in Figure 8 left, $10^{19.7}$ eV (purple dotted line) and 10^{20} eV (purple solid line), which are also displayed as sky exposures in Figure 9 in declination versus right ascension. In in Figure 9 the color scale denotes the exposure variations in terms of the mean response taking into account the positions of the sun and the moon during a 5-year observation cycle. The higher exposure

for limb observations is also clear in Figure 8 left as red lines for three energies: 10^{20} eV (dotted), $10^{20.3}$ eV (dashed), and 10^{21} eV (solid).

POEMMA will measure the UHECR source distribution on the full celestial sphere under a single experimental framework with a well-defined UHECR acceptance, mitigating the issues of cross-comparisons inherent to viewing different portions of the sky with multiple experiments. The response shown in Figure 9 was calculated assuming a configuration of the POEMMA telescopes pointing near the nadir. The ability of the space-based POEMMA telescopes to tilt towards the northern or southern hemisphere allows for the sky exposure can be enhanced for a specific hemisphere. Likewise, it is easy for POEMMA to view north or south for a sequence of orbital periods to further tailor the UHECR sky coverage for possible source locations.

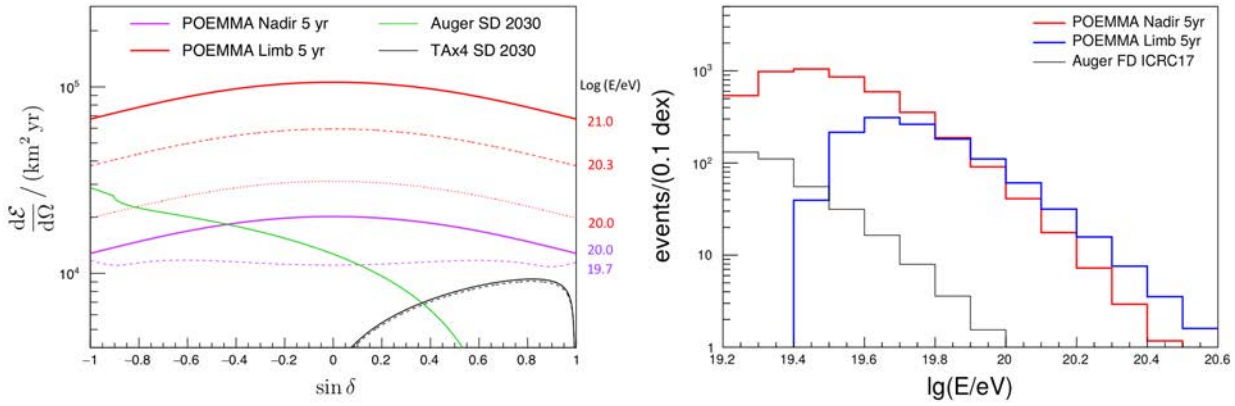

FIG. 8: Left: Differential exposure as a function of declination for five years of POEMMA operations in nadir mode (purple lines) and two energies for EASs: $10^{19.7}$ eV (dotted) and 10^{20} eV (solid); and for limb mode (red lines) and three energies: 10^{20} eV (dotted), $10^{20.3}$ eV (dashed), and 10^{21} eV (solid). The exposures of Auger and TA (including the TAx4 upgrade) are shown as black (TA) and green (Auger) lines respectively assuming operations until 2030. Right: Number of UHE events detected by POEMMA for five years of observations in nadir (red) and limb (blue) operational mode respectively. For comparison, the current event numbers of the Auger *fluorescence* observations indicated by black lines.

Figure 10 left shows an example of a 5-year stereo UHECR exposure in terms of the Auger and TA exposures reported in 2017 [7]. The POEMMA UHECR exposures are calculated from simulations assuming an isotropic flux and an EAS trigger condition based on the modeling of the response of the PDMs in the PFC [49]. Simulations of the EAS reconstruction selection criteria lead to an 85% acceptance for stereo mode and 80% for the tilted (monocular) configuration for UHECR observations in neutrino mode. The fraction of time POEMMA is viewing the night sky with minimal moonlight is 18% based on calculations for the POEMMA orbit [48]. Previous simulation studies [49] have shown that 72% of events observed from space have the location of shower maximum above clouds based on meteorological cloud height measurements. An additional 5% reduction to account for the effects of light pollution from cities and lightning. These lead to an effective duty cycle of 12% for the UHECR aperture determined after event reconstruction selection.

When POEMMA is operating in limb observing mode (see Figures 2 right), the two

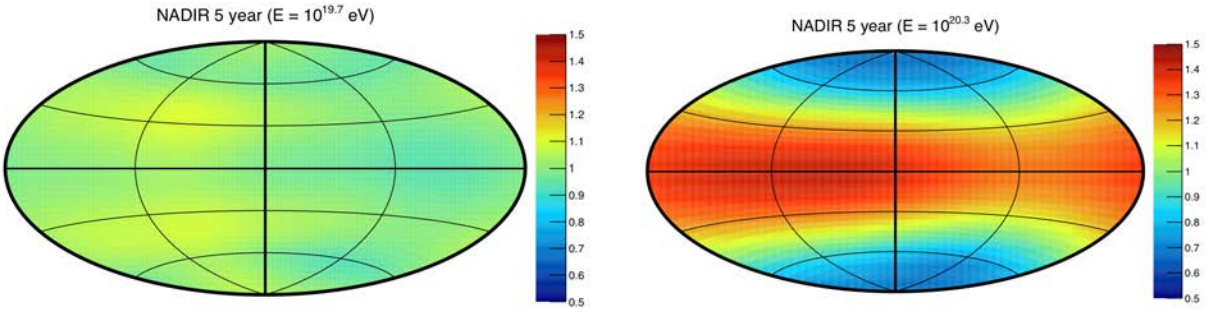

FIG. 9: POEMMA UHECR sky exposure for nadir observations in declination versus right ascension. Color scale denotes the exposure variations in terms of the mean response taking into account the positions of the sun and the moon during a 5-year observation cycle. Left: Sky exposure for showers of $10^{19.7}$ eV. Right: Sky exposure for showers of 10^{20} eV.

satellites are separated by ~ 30 km and tilted up to 47° away from the nadir to view the limb of the Earth. Consequently, the UHECR asymptotic aperture increases by nearly an order of magnitude, albeit with a higher UHECR energy threshold for reconstructing the observed events (see Figure 10 left). With the smaller satellite separation, the performance is closer to monocular reconstruction, where the 1 μs timing information is needed in order to yield a measurement on orientation of the EAS in the atmosphere. While the monocular performance in terms of angular (few degree resolution near 100 EeV) and composition ($X_{\rm max}$ ~ 100 g/cm^2) resolution is not as accurate as that for the stereo mode, the energy resolution is still ~ 20%. This energy resolution and the significant increase in statistics (see Figure 3) allows for the unique study of the spectral shape above 100 EeV and the sky distribution of UHECRs with the highest rigidity.

POEMMA is designed to be able to perform both stereo and monocular reconstruction of the fluorescence signal, with the latter being needed for risk mitigation in the case that one satellite fails to perform properly. In addition, POEMMA will observe 2° above the limb to measure UHECR Cherenkov signals [50] as it monitors below the limb for cosmic neutrinos (as discussed in VI below).

D. Cosmic Neutrino Science

POEMMA will provide measurements of key components of extreme energy multi-messenger astrophysics. In addition to the study of the many components of UHECRs above 20 EeV, the POEMMA design adds the capability of searching for neutrinos above 20 PeV (1 PeV ≡ 10^{15} eV) from ToO events. (Note that above 10 PeV, the neutrino and anti-neutrino quark scattering cross sections are virtually identical, and we denote neutrinos and anti-neutrinos simply as neutrinos.)

POEMMA is unique in the ability to follow-up transient events on time scales of order one orbit (95 min) over the entire dark sky and over the full sky on time scales of months. Since no prompt neutrinos have been observed at these energy scales, POEMMA will discover which transient events produce very-high energy neutrinos and at what times after the event.

Very high-energy cosmic neutrinos are emitted in a number of models of astrophysical transient events, such as gravitational wave events from neutron-star binary coa-

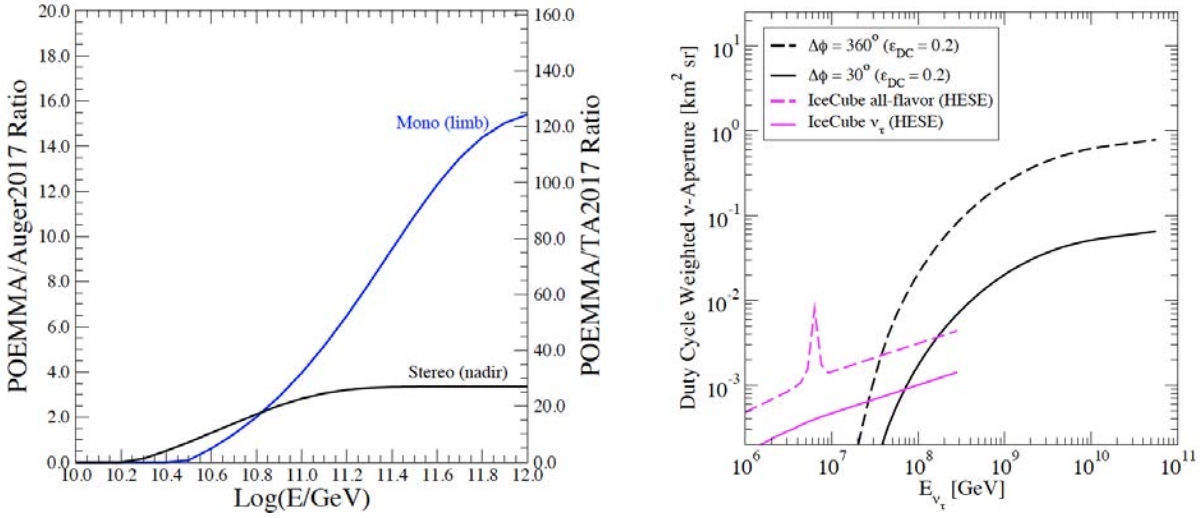

FIG. 10: Left: Examples of the 5 year POEMMA stereo UHECR exposure for a satellite separation of 300 km, assuming a 10% duty cycle, in terms Auger exposure [7] and TA until ICRC-2017. The Stereo (Mono) mode has lower (higher) energy threshold and exposure. Right: POEMMA diffuse-flux neutrino aperture as a function of ν_τ energy for accepting ν_τ's through the up-going τ-lepton decay EAS. Solid-line for current design with 30° FoV in Cherenkov and dashed-line for POEMMA360, (design with FoV 360°), and Duty Cycle ε_{DC} of 20%. Also shown IceCube all-flavor (dashed line) and ν_τ (solid line) neutrino aperture for HESE (high-energy starting events).

lescence [51, 52], short and long gamma-ray bursts, the birth of pulsars and magnetars, fast-luminous optical transients [53], blazar flares (e.g., TXS 0506+056 [54]), and possibly many other high-energy transients. POEMMA can follow up these events and reach a neutrino fluence around $E_\nu^2 J_\nu \geq 0.1$ GeV/cm^{-2} depending on the location of the sources (see Figure 14 and [55]).

In models of cosmic neutrino emission, neutrinos are generally produced in the decay of pions, kaons, and secondary muons generated by hadronic interactions in astrophysical sources. Consequently, the expectation for the relative fluxes of each neutrino flavor at production in the cosmic sources, $(\nu_e : \nu_\mu : \nu_\tau)$, is nearly $(1 : 2 : 0)_{source}$. After neutrino oscillations decohere over astronomical propagation distances the flavor conversion is properly described by the mean oscillation probability. As a result, cosmic neutrinos should arrive on Earth with democratic (maximally mixed) flavor ratios, $(1 : 1 : 1)_\oplus$, for most extragalactic sources [56]. POEMMA will observe in general one third of the generated neutrino flux via the ν_τ flux.

High-energy neutrinos can be produced by a variety of astrophysical sources, including the unknown UHECRs sources and the propagation of UHECRs from extragalactic sources to Earth. The interactions of UHECRs with the cosmic microwave (GZK effect) and infra-red backgrounds lead to a cosmogenic neutrino flux from the decay of pions and neutrons [57, 58]. The cosmogenic flux depends on the nuclear nature of the primaries [59–68] providing another measure of the UHECR composition [66, 69]. Given the current data on UHECR composition, the diffuse cosmogenic neutrino flux is too faint for POEMMA to reach with its 30° effective FoV Cherenkov camera design described here. The POEMMA collaboration is developing a version of the POEMMA mission with 360° FoV, named POEMMA360, which will be sensitive to the diffuse neutrino flux (see Figure

10 right).

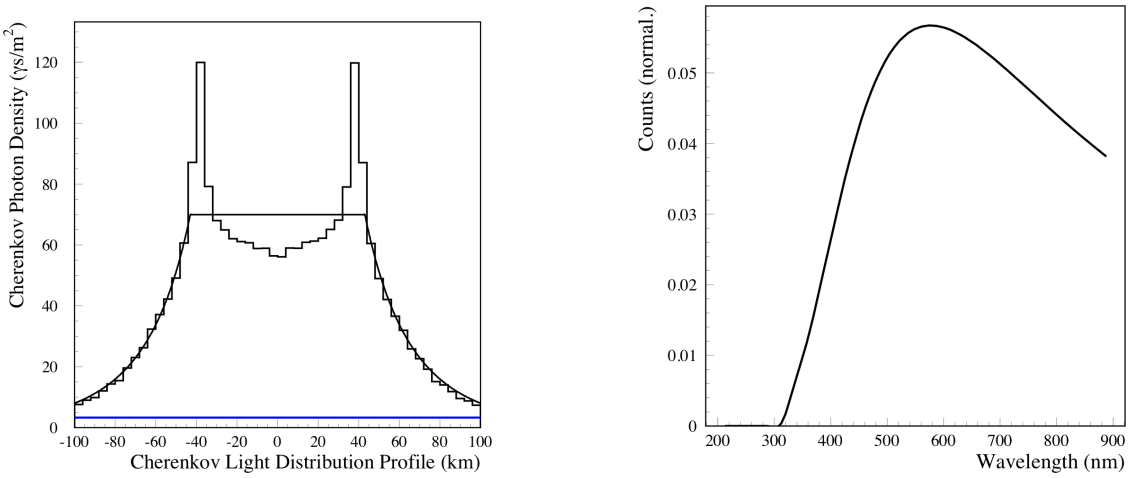

FIG. 11: Left: The spatial profile of the Cherenkov signal (photons/m^2) at 525 km altitude for a 100 PeV upward EAS with a 10° Earth emergence angle. Right: The simulated Cherenkov spectrum observed by a POEMMA observatory.

E. POEMMA Cosmic Neutrino Performance

POEMMA's sensitivity to ν_τ's is based on the observation of Cherenkov emission from EAS caused by the decay of τ-leptons as they exit the Earth's surface. Observable τ-decay events for POEMMA start in directions close to the limb of the Earth located at 67.5° from the nadir for POEMMA's 525 km altitude. The geometry of the τ emerging angles with respect to the Earth's surface (θ_e) and the corresponding observing angle below the limb for POEMMA (δ) are defined in Figure 12. Assuming Standard Model interactions and observable energies, the Earth emergence angles tend to be below $\theta_e \lesssim 35°$ corresponding to POEMMA observations with $\delta \lesssim 18.3°$ below the limb. (A complete study of the geometry and the corresponding sky coverage of neutrino induced Cherenkov events observable by POEMMA can be found in [48].)

Numerical simulations indicate that the Cherenkov light profile at POEMMA is essentially a flat top with width of tens of km and with a power law falloff (as shown in Figure 11 left). This motivates the satellite separation for neutrino mode to be $\sim$ 30 km in order for both satellites to observe a significant portion of the light pool of the same event. The POEMMA photometer focuses the Cherenkov signal in a pixel with some spread due to the point-spread-function (PSF) of the optics. Simulations also show that the accepted upward τ-lepton induced EAS has a temporal width of $\sim$ 20 ns, defining the sampling time for the POEMMA Cherenkov Camera (PCC) (the SiPM portion of the focal plane). Using a coincidence window of 60 ns results in a false positive Cherenkov signal of $\sim$ 0.1%, due to the atmospheric air glow background, with sensitivity to ν_τ down to $\sim$ 20 PeV.

Figure 10 right shows the diffuse-flux neutrino aperture for POEMMA as a function of ν_τ energy assuming a 20% duty cycle. The current POEMMA design surpasses IceCube HESE (high-energy starting events) [70] above 70 PeV for diffuse neutrino flux searches.

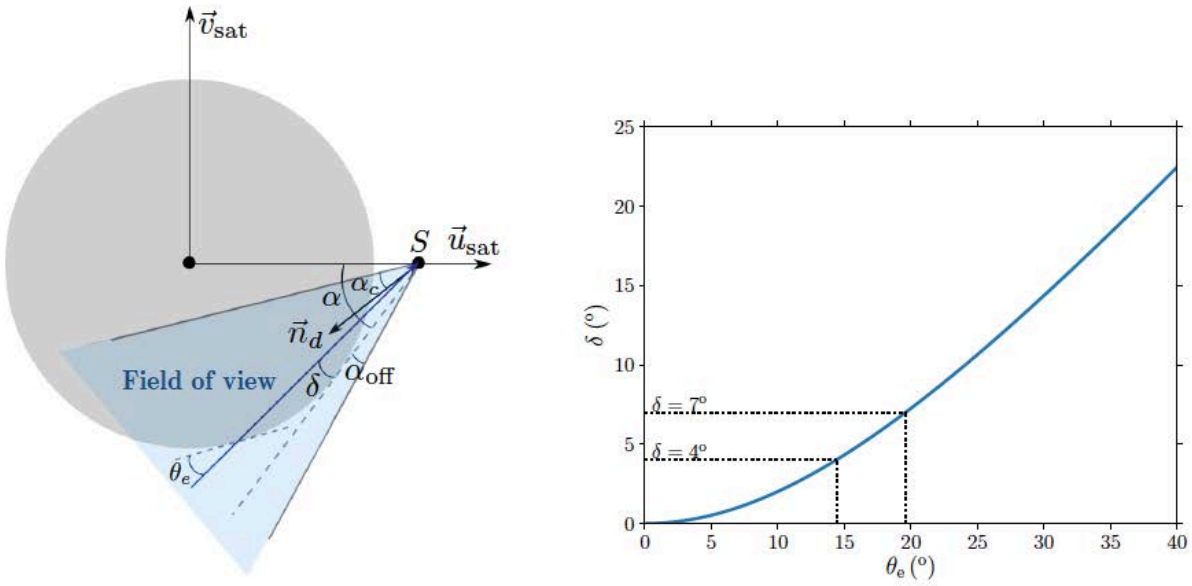

FIG. 12: Left: Illustration of the geometrical configuration in the orbital plane (satellite position, $\vec{u}_{\rm sat}$, versus satellite velocity $\vec{v}_{\rm sat}$). The satellite is located at point S. The direction of arrival of an EAS generated by a ν_τ is characterized by its Earth emergence angle θ_e and the corresponding viewing angle from the satellite point of view δ below the limb. The detector has a conical FoV of opening angle α_c, with an offset angle $\alpha_{\rm off}$ (away from the Earth limb) and pointing direction $\vec{n}_d$. Right: Cherenkov viewing angle δ below the limb versus Earth emerging angle θ_e [48].

The results are shown for two cases, one with an azimuth angle span of 30°, which corresponds to the current conceptual design for POEMMA, and the 360° azimuth viewing for POEMMA360. The benefit of increasing the azimuth range of the limb observations is clear and will drive the development for the eventual POEMMA mission. For ToO searches, the current POEMMA design is an order of magnitude more sensitive as shown in Figure 14.

Figure 13 left shows the fraction of τ-leptons over the flux of ν_τ's as a function of τ-energy for Earth emerging angles $\theta_e = 1°, 5°, 10°, 20°$ for a cosmogenic flux from ref. [66]. These results are based on a new calculation developed under the POEMMA probe study [71]. The new ν_τ interaction and τ-lepton energy loss modeling uses a layered density of the Earth based on the Preliminary Reference Earth Model [72]. The ν_τ's create τ-leptons in charged-current interactions with nucleons in the Earth. At the high energies of interest for POEMMA, the resulting τ-leptons lose energy while propagating through the Earth and have a finite probability of escaping the Earth in an energy-dependent way. The process is complicated by ν_τ regeneration [71, 73]: τ-leptons that decay in the Earth produce lower energy ν_τ's that then can interact in the Earth. The figure shows the effect of the different column depths (which increase as the Earth emergence angles θ_e increase) on the energy spectrum of emerging τ-leptons. Since the Standard Model neutrino cross section increases with energy [74], smaller column depths (smaller θ_e) increase the sensitivity to higher energy neutrinos. Larger column depths are most sensitive to lower energy neutrinos, but with a contribution from higher energy ν_τ's through regeneration [73].

Once the τ-lepton escapes the Earth, an EAS model is used to develop the EAS cascade, generate the beamed Cherenkov light, and attenuate the light using an atmospheric

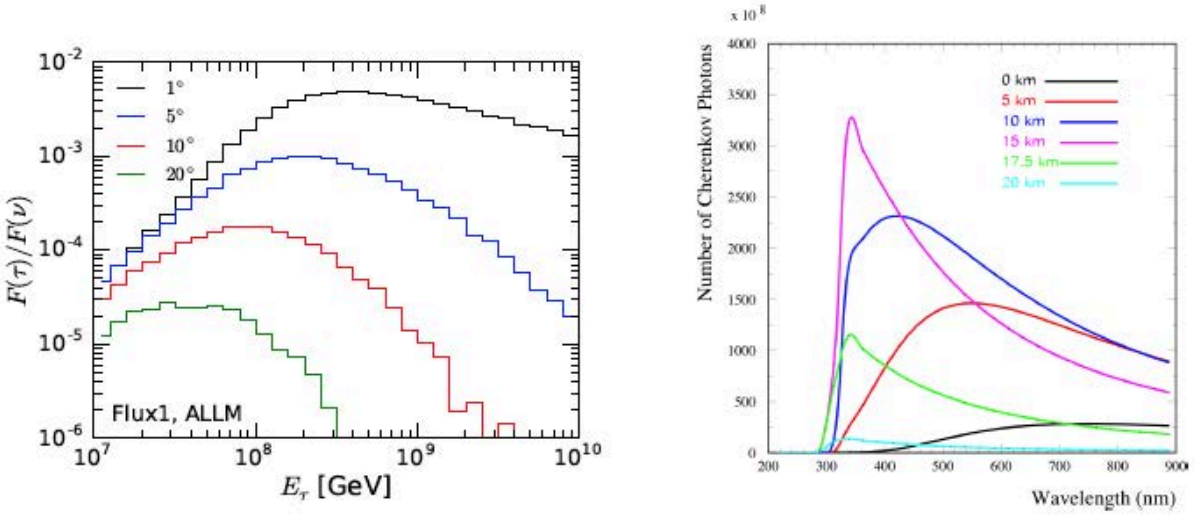

FIG. 13: Left: The fraction of τ-leptons over an incoming flux of ν_τ's as a function of τ-energy for Earth emerging angles $\theta_e = 1°, 5°, 10°, 20°$ [71]. (ALLM refers to the energy loss model in [71] and the cosmogenic flux is from [66].) Right: Cherenkov signal intensity as function of wavelength for 100 PeV upward-moving EASs for $\theta_e = 5°$ Earth emergence angle as a function of EAS starting altitude [71].

model that includes the wavelength dependent attenuation due to aerosols, Rayleigh scattering, and ozone absorption. The interplay between the τ-lepton Earth-emergence angle, τ-lepton energy (and hence decay altitude), the Cherenkov light generation, and atmospheric absorption determines the observability of an upward-moving EAS. For example, while Figure 13 left shows a significant flux of sub-100 PeV τ-leptons for smaller Earth-emergence angles, these decay at very low altitudes and the Cherenkov light gets strongly absorbed by the low-altitude aerosols.

Figure 13 right illustrates the observability of a τ-lepton as a function of altitude for a fixed EAS τ energy and Earth emergence angle $\theta_e = 5°$. The Cherenkov intensity and wavelength dependence are very sensitive to the starting altitude. At the lowest altitudes, aerosol absorption dampens the Cherenkov intensity and pushes the spectrum towards the longest wavelengths. As the starting altitude increases, the exponential nature of both the aerosol layer and atmosphere itself leads to EAS higher Cherenkov intensities and spectra peaked at lower wavelengths. At even higher altitudes the atmosphere becomes too rarified for complete EAS development, leading to a reduction in the Cherenkov intensity for EAS developing above 17 km altitudes.

As in the air fluorescence case, the brightness of the beamed Cherenkov signal compared to the airglow background sets the energy threshold for observation. The peak of the Cherenkov spectrum spans the $300 < \lambda/\text{nm} < 900$ band due to the dependence of atmospheric absorption on column depth and Earth emergence angle. The airglow background is stronger in this wavelength band than for the UV fluorescence case. The airglow spectrum and intensity toward the limb sets the energy threshold for the Cherenkov signals.

POEMMA observes the upward-moving EAS within a few degrees from the EAS propagation direction (see Figure 4). Simulations show that the time width of the Cherenkov signal for accepted events is $\lesssim 20$ ns. Simultaneously viewing of the τ decay EAS with

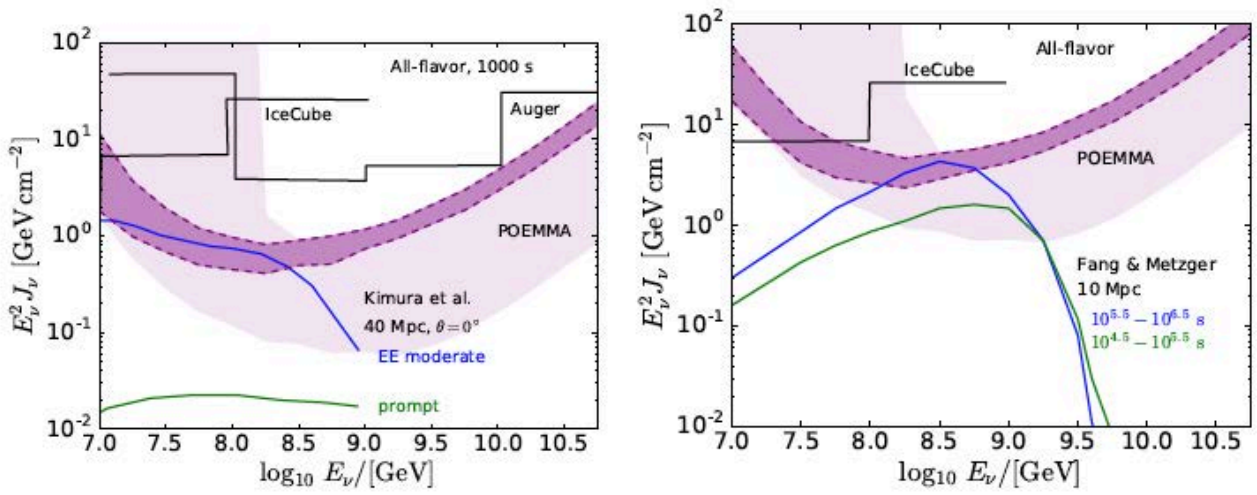

FIG. 14: POEMMA ToO sensitivities to a short, 1000 s burst (left) and long (right) bursts shown by the purple band, where the dark purple bands correspond to source locations between the dashed curves in the sky coverage Figure 15. Also shown are, left: The IceCube and Auger sensitivities (solid histograms), scaled to 3 flavors for ±500 s around the binary neutron star merger GW170817 [75], and the Kimura et al. [52] all flavor fluences for extended emission (EE) and prompt emission from a short gamma ray burst, scaled to $D = 40$ Mpc, for on-axis viewing ($\theta = 0°$). Also shown right: The IceCube sensitivity (solid histogram), scaled to three flavors, for a 14 day time window around the binary neutron star merger GW170817 [75] and the all-flavor fluence predictions for millisecond magnetars from Fang & Metzger [51] for a source distance of $D = 10$ Mpc for time intervals of $10^{5.5} - 10^{6.5}$ s and $10^{4.5} - 10^{5.5}$ s.

both POEMMA satellites reduces the false positive rate due to the airglow background, yielding a better sensitivity to cosmic ν_τ's below 100 PeV.

POEMMA's exposure for cosmic ν_τ sources for one orbital period traces out a band on the celestial sky defined by the inclination of the orbit and the off-orbit angle the telescopes point. Figure 15 left shows the sky coverage for a given day of the year for sources located by the sine of the declination and right ascension, without including the effect of the Sun, for viewing angles 0 to $\delta = 18.3°$ below the limb [55]. Some sources are located in sky positions that never set below the horizon (shown in white in Figure 15 left) and will only be observed when the Earth's orbit brings that part of the sky into cosmic neutrino view. The majority of the sky positions in Figure 15 left are for sources that set and rise at angles close to the orbital plane. A few areas in the sky have one order of magnitude more sensitivity because their rising and setting are at very oblique angles to the horizon: these are shown in the darker red colors in Figure 15 left.

Different models of neutrino emission for astrophysical transients predict short and long term cosmic neutrino emission after the transient. To search for a short term cosmic neutrino burst, POEMMA can reorient its viewing angle in a few minutes and revisit the same location once an orbit afterwards. For longer period emissions, POEMMA can monitor the location of a given transient months after its multi-wavelength discovery. Figure 14 displays the POEMMA fluence sensitivity for short and long cosmic neutrino emission depending on the source location. The purple bands show the range of sensitivities accessible to POEMMA. In Figure 14 left the sensitivity is for short bursts of 1000 s assuming sources are in the observable part of the sky. The dark purple band corresponds

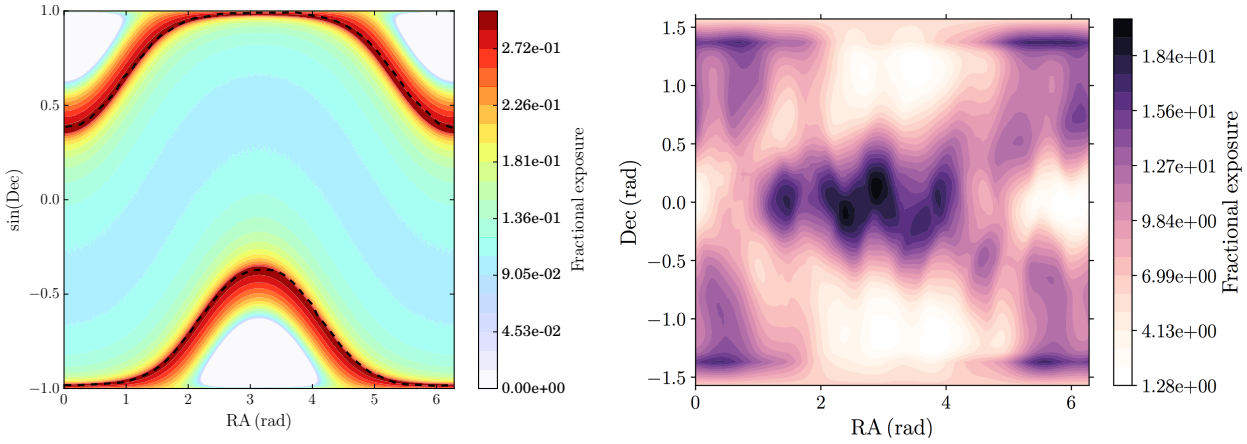

FIG. 15: POEMMA cosmic neutrino sky coverage Left: Sky coverage for sources at a given orbital position in the sine of the declination and right ascension, without including the effect of the Sun, at a given time of the year for viewing angles to $\delta = 18.3°$ below the limb [55]. Right: The fractional neutrino sky exposure for one year in declination versus right ascension, assuming a defined variation in the POEMMA limb-pointing directions over the year to achieve full-sky coverage. The calculation takes into account the effects of the sun and moon on the duty cycle for observations [48].

to source locations between the dashed curves in the sky coverage plot in Figure 15 left. The IceCube and Auger sensitivities, scaled to 3 flavors for ±500 s around the binary neutron star merger GW170817, are shown with solid histograms [75] for comparison. Also plotted in Figure 14 left are predictions from Kimura et al. [52] all flavor fluences for extended emission (EE) and prompt emission from a short gamma ray burst, scaled to $D = 40$ Mpc, for on-axis viewing ($\theta = 0°$).

Figure 14 right shows the POEMMA sensitivity for long bursts. The IceCube sensitivity, scaled to three flavors, for a 14 day time window around the binary neutron star merger GW170817 is shown with the solid histogram [75]. Also shown are all-flavor fluence predictions for millisecond magnetars from Fang & Metzger [51] for a source distance of $D = 10$ Mpc for time intervals of $10^{5.5} - 10^{6.5}$ s and $10^{4.5} - 10^{5.5}$ s.

Figure 15 right shows the one year ν_τ sky coverage, based on a specific set of defined repoints for each orbital period, demonstrating the ability to cover the full sky yearly [48]. The figure illustrates the unique capability of POEMMA to adjust its observing strategy to benefit from the flexibility of space-based observations to follow cosmic neutrino sources over the full sky. An in-depth analysis of the best cosmic neutrino target for POEMMA should optimize repoints during a given observational period giving priority to the most likely high-energy neutrino sources to be followed-up as ToOs for different time windows after each transient.

F. Beyond the Standard Model Physics

POEMMA will be a powerful probe of physics beyond the Standard Model of particle physics such as neutrinos emission from relics from the very early universe. An example involves the flux of extremely high energy cosmic neutrinos produced via decay of

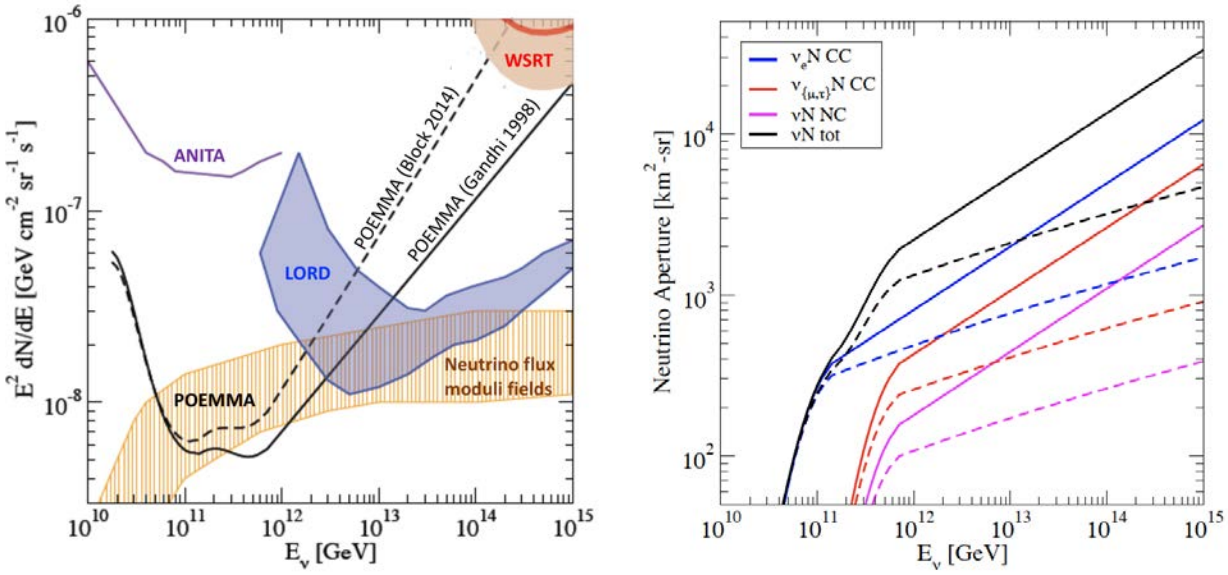

FIG. 16: POEMMA sensitivity to EAS showers produced by neutrinos interacting in the atmosphere and observed via fluorescence. Left: Black curves are POEMMA sensitivity using [76] (solid) and [74] (dashed) cross sections. Predictions for strongly coupled string moduli (orange range) [77], LORD sensitivity (blue band) [78], ANITA I-IV limits (purple) [79], and WSRT [80]); Right: POEMMA neutrino aperture from fluorescence with [76] (solid) and [74] (dashed) cross sections for CC interactions: ν_eN (blue), ν_μ and ν_τ (red); NC interactions (pink); and total (black).

highly boosted (strongly coupled) moduli, radiated by relic cosmic strings [77]. These strongly coupled moduli are scalar fields, which appear to be quite generic in the string theory landscape [81, 82]. Another example is the possibility that extremely high energy neutrinos could originate in the decay of superheavy dark matter (e.g., [83]).

In Figure 16 we show the sensitivity of both POEMMA and the future Lunar Orbital Detector (LORD) [78], and current limits from ANITA I-IV [79] and WSRT [80]. We also show the neutrino flux range resulting from models of strongly coupled moduli in a string theory background with $G\mu \sim 10^{-20}$, where G is the Newton's constant and μ the string tension [77]. POEMMA sensitivity was estimated assuming the stereo configuration observations with 10% duty cycle and 5 years of observation time. The neutrino aperture is the result of simulations of isotropic events interacting deep in the atmosphere (starting point > 1500 g/cm^2). The sensitivity includes all flavors, charged and neutral current interactions, for two different cross-sections, [76] and [74].

It is evident that POEMMA will probe a significant part of the parameter space, providing a method of searching for strongly coupled moduli, which complements searches based on gravitational effects of strings, like structure formation, cosmic microwave background, gravitational radiation, and gravitational lensing. The strongest current bound from lensing effects is estimated to be $G\mu \lesssim 10^{-7}$ [84], while millisecond pulsar observations lead to $G\mu \lesssim 4 \times 10^{-9}$ [85]. Next generation gravitational wave detectors are expected to probe $G\mu \sim 10^{-12}$ [86, 87]. Thus, POEMMA will attain sensitivity to a region of the parameter space more than 10 orders of magnitude below current limits and about 8 order of magnitude smaller than next generation gravitational wave detectors.

Another test of BSM physics is the search for protons, neutrons [88], and photons, from

sources that are too far for the observed energies. Such observations related to a spectral recovery past the GZK effect will test theories that violate Lorentz invariance (for a review see, e.g., [89]).

A recent BSM possibility was the report by the ANITA experiment of two intriguing up-going showers with deposited energies in the range $10^8 \lesssim E/\mathrm{GeV} \lesssim 10^9$ [90, 91]. These events could originate in the atmospheric decay of an up-going τ-lepton produced through a charged current interaction of a ν_τ inside the Earth. However, the relatively steep arrival angles of these perplexing events create tension with the standard model (SM) neutrino-nucleon interaction cross section: : the projected column depth through the Earth for these events is approximately 10 times the neutrino interaction length. The lack of similar observations from Auger and IceCube implies that the messenger particle giving rise to ANITA events must produce an airshower event rate at least a factor of 40 larger than that produced by a flux of τ-neutrinos [92]. The ANITA events might have a new physics origin. Theorists have had no problem coming up with ideas [93–101], but the origin of ANITA τ-lepton event candidates remains a mystery.

G. Atmospheric Science

POEMMA will be the most sensitive instrument to transient luminous events than any instrument flown to date. The largest instrument flown so far is the TUS experiment on the Lomonosov Satellite [102]. The larger FoV and aperture makes POEMMA 23.4 more likely to observe a TLE than TUS. At present the following TLEs have been identified in the upper atmosphere: Jets, SPRITES, ELVES, and TEBs.

Jets are the brightest TLEs and are caused by terrestrial lightening discharges that go upward to altitudes as high as 70 km. They present in several different forms, blue jets, blue starters and gigantic jets. Jets last 0.1 to 1 second.

SPRITES (Stratospheric/mesospheric Perturbations Resulting from Intense Thunderstorm Electrification) are the result of positive cloud-to-ground lightening. They are caused by atmospheric gravity waves that grow in the electric fields produced by lightning. Sprites occur in the mesosphere at 50 to 90 km altitude. Their appearance varies and their color ranges from blue to red. They last 10 to 100 ms.

ELVES (Emission of Light and Very Low Frequency perturbations due to Electromagnetic Pulse Sources) often appear as a dim, flattened, expanding glow around 400 km in diameter that lasts for, typically, just one ms, but can be as short as [102] 30 μs. They are produce when an electromagnetic (EM) pulse from [102] cloud-to-ground lightening propagates into the ionosphere at an [102] altitude of $\sim$ 100 km. They typically appear as expanding rings or [102] ovals (depending on the inclination of the initiating lightning bolt). These features expand at superluminal speeds because they occur at the intersection between the spherical EM pulse and the ionosphere.

TEBs (Terrestrial Electron Beams) are predicted to be injected into the magnetosphere by terrestrial gamma-ray flashes. These electrons would be guided by the Earth's magnetic field toward the conjugate point in the opposite hemisphere where some would re-enter the atmosphere while others would mirror and return to their point of origin. While phenomenon is yet to be detected, when the electrons enter the atmosphere, they will generate atmospheric fluorescence flashes lasting 1 to 10 ms.

The set of TLEs described above can be easily identified by POEMMA given their morphology and time evolution. For example, the fast timing and light gathering power

of POEMMA is well-suited to measure elves in detail. ELVES carry signatures of fundamental properties of high-current lightning [103]. High-current lighting is produced by extremely strong convective thunderstorms. These destructive storms are becoming more frequent and severe as the climate warms [104–106]. Studies of the properties of strong convective storms of today offer a proxy to study extreme storms of the future.

H. Meteors and Nuclearites

Meteor and fireball observations are key to the derivation of both the inventory and physical characterization of small solar system bodies orbiting in the vicinity of Earth. POEMMA will be able to detect meteors down to absolute magnitude close to 8 given POEMMA's large FoV and good sensitivity, based on similar studies performed in the framework of the JEM-EUSO (Joint Experiment Missions for Extreme Universe Space Observatory) program [107, 108]. Thus POEMMA will record a statistically significant flux of meteors, including both sporadic ones, and events produced by different meteor streams. Being unaffected by adverse weather conditions, POEMMA can also be a very important facility for the detection of bright meteors and fireballs, as these events can be detected even in conditions of very high sky background, and thanks to the stereoscopic vision, derive a 3D reconstruction of the meteor trajectory.

Moreover, the observing strategy developed to detect meteors may also be applied to the detection of nuclearites, exotic particles whose existence has been suggested by some models [109]. Nuclearites are expected to move at higher velocities than meteoroids, and to exhibit a wider range of possible trajectories, including particles moving upward after crossing the Earth. The analysis performed for JEM-EUSO, and re-scaled for POEMMA, indicates that POEMMA will be sensitive to nuclearites with mass higher than 10^{22} GeV/c^2. Even in case of a null detection, after 1 year observation, POEMMA would be able to provide a limit to their flux, which is 3 orders of magnitude more stringent lower than those obtained so far by previous experiments [110, 111].

III. POEMMA INSTRUMENT

The design of the POEMMA instruments (Figure 1) and mission evolved from previous work on the OWL [112] and JEM-EUSO [49] designs, the CHANT concept [113], and the sub-orbital payloads EUSO-SPB1 [114] and EUSO-SPB2 [115]. POEMMA is composed of two identical space-based platforms that provide significant advantages in terms of exposure and sky coverage to discover the origin and nature of UHECRs. The two POEMMA observatories detect extreme energy particles by recording the signals generated by EASs in the night side of the Earth's atmosphere.

Extensive air showers develop at speeds close to the speed of light with particle distribution profiles reaching tens of kilometers at ultra-high energies (see Figure 4 left). The central element of each POEMMA observatory is a high sensitivity low resolution photometer that measures and locates two types of emission from these EASs: the faint isotropic emission due to the fluorescence of atmospheric nitrogen excited by air shower particles (with emission in the $300 \lesssim \lambda/\text{nm} \lesssim 500$ range, Figure 4 right), and the bright collimated Cherenkov emission from EASs directed at the POEMMA observatory (with light distribution and emission spectrum as in Figure 11). POEMMA optics and cameras

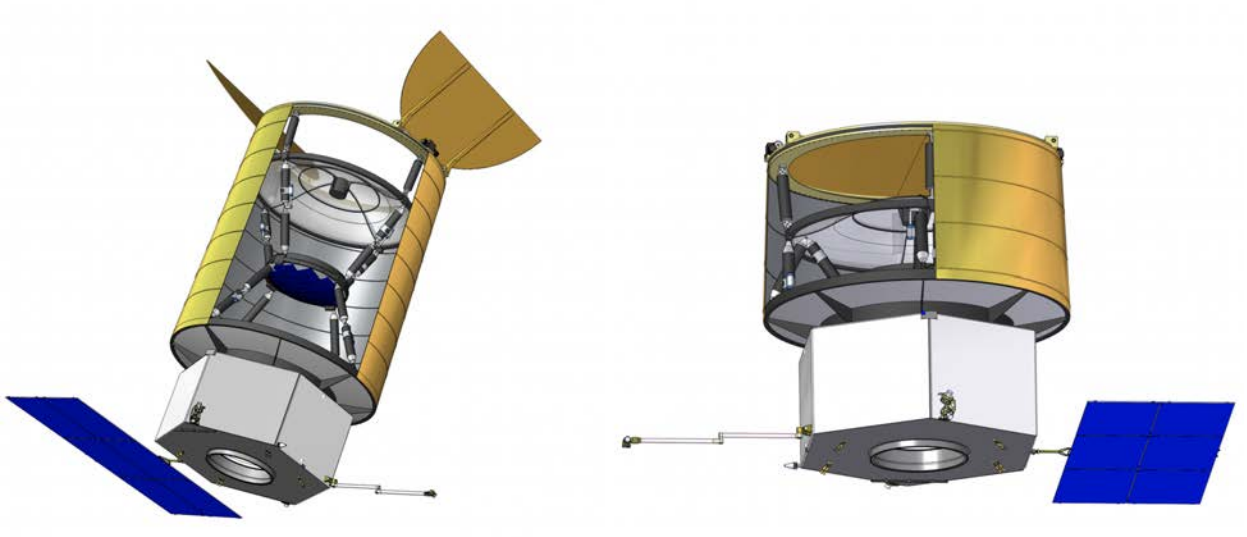

FIG. 17: POEMMA observatory (photometer and spacecraft) deployed with open shutter doors (left) and in stowed position for launch (right). Cutaways in the light shield display the internal structure of corrector plate and focal surface in the middle of the payload (blue). Spacecraft bus shown with solar panel (blue) and communications antenna deployed in both images.

are designed to optimize the wavelength coverage, time gate, and pixel sizes to best reconstruct ultrahigh energy EASs.

The POEMMA photometer design results from an intense work session at the Instrument Design Laboratory (IDL) at the Integrated Design Center (IDC) at the Goddard Space Flight Center (GSFC) from July 31 to August 4, 2017. Following the IDL study, the POEMMA Study Team (ST) and key technical personnel at Marshall Space Flight Center (MSFC) de-scoped the design (simplifying and down-sizing the optics system) to arrive at a balance between science objectives and resources.

Each POEMMA photometer features a large diameter optical system (mirror and corrector plate, see Figure 1 and 18) to collect the fluorescence and Cherenkov signals. Photons are focused onto a coarsely segmented focal surface (Figure 21) and subsequently digitized as short videos of fluorescence traces (Figure 20 right) and Cherenkov light pulses. These signals are focused on different regions of the focal surface for each measurement type. Cherenkov photons are observed just over the horizon (for UHECRs) and below the limb (for cosmic neutrinos) and focused in the region near the edge of the focal surface on the PCC. On the bulk of the focal surface, fluorescence photons are recorded by the POEMMA Fluorescence Camera (PFC). The design for each region is tailored to the measurement required by the science investigation.

The instrument architecture incorporates a large number of identical parallel sensor chains that meet the high standards of a Class B mission. Aerospace grade components have been identified for key elements within these sensor chains to insure reliability for the mission. The highest risk element is the shutter doors that must open and close each orbit. The approach developed in the IDL for the shutter relies on a simplified design to address the Class B risk designation through redundancy and ground-based testing. All remaining critical subsystems in the instrument and spacecraft (S/C) are fully redundant

to achieve a low risk mission profile.

The photometers are designed for deployment after launch. A stowed configuration (see Figure 17) enables two identical satellites to be launched together on a single Atlas V rocket (see Figure 25). Space qualified mechanisms extend each instrument after launch to their deployed position to begin observations.

The functionality of key elements of the instrument is described below. The resulting concept meets performance requirements and fits within the resource constraints.

A. Optics

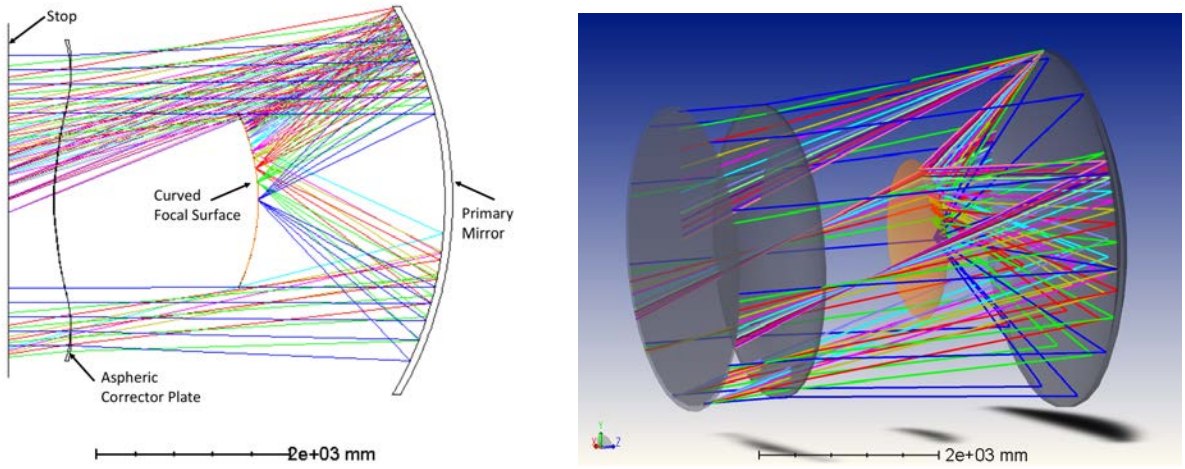

FIG. 18: Left: Cross sectional layout of POEMMA optics. Right: Model of POEMMA optics.

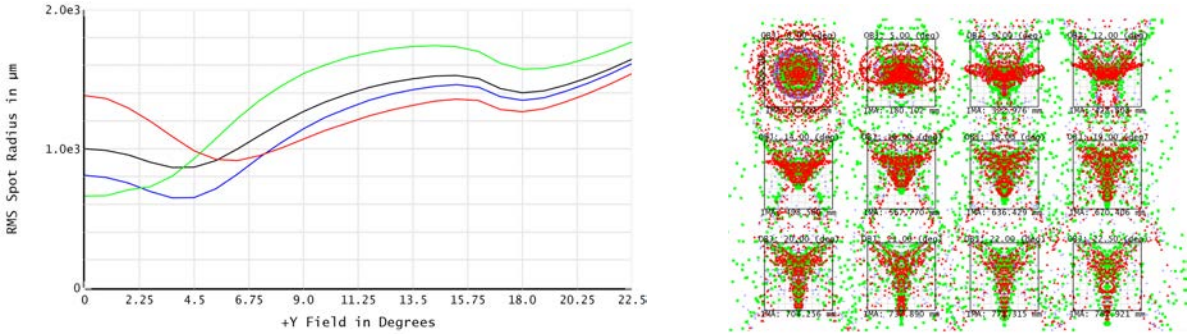

FIG. 19: Left: RMS of the spot radius as a function of incident angle, plotted for polychromatic (black) 0.36 (blue) 0.33 (green) and 0.39 (red) microns. Right: Spot diagram, over 45 degree FoV, plotted against 3 mm pixel size areas; dots for 0.36 (blue) 0.33 (green) and 0.39 (red) microns.

The POEMMA photometer is based on a Schmidt photometer (see Figure 18) with a large spherical primary mirror (4 m diameter), the aperture and a thin refractive aspheric aberration corrector (3.3 m diameter) at its center of curvature, and a convex spherical focal surface (1.61 m diameter). This particular system provides a large collection aperture (6.39 m^2) and a massive field-of-view (45° full FoV).

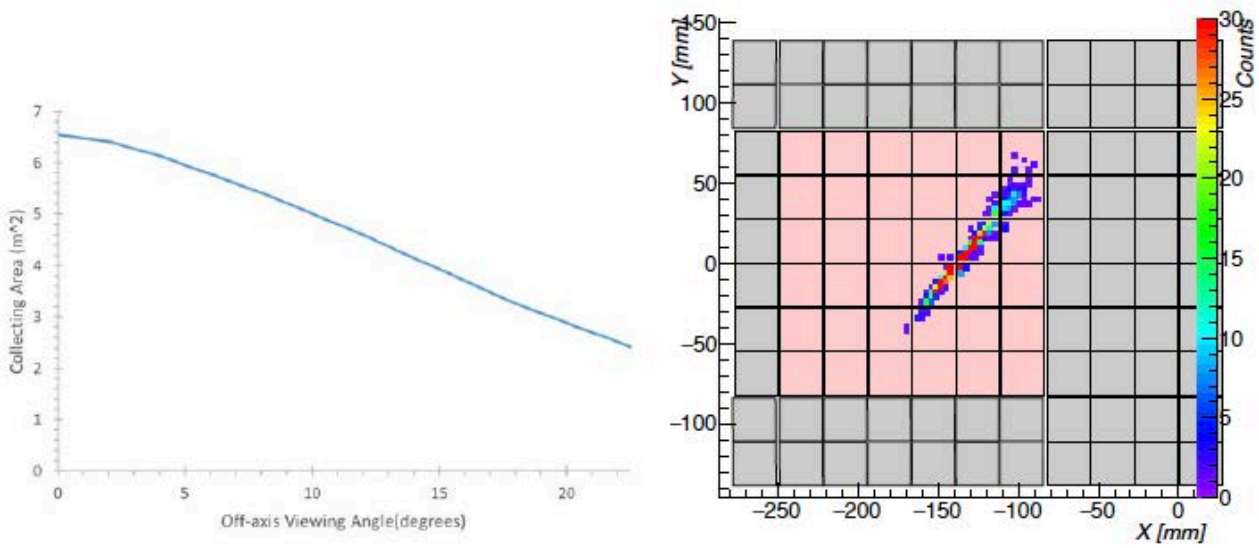

FIG. 20: Left: POEMMA optics effective area as a function of viewing angle. Right: EAS fluorescence image on one POEMMA Photo Detector Module (PDM) for a 100 EeV shower.

To accurately resolve the EAS development, we require a spatial resolution of ~ 1 km from 525 km, which leads to pixel angular resolution of ~ 0.1° or smaller. Given the 3 mm pixel size of the focal surface, the optics design achieves an instantaneous FoV of 0.084 degrees per pixel and results in a system with an effective focal length, EFL = 2.04 m, and an effective pupil diameter, EPD = 3.3 m. Because the image, and therefore the detectors, are located between the aperture and the mirror, they obscure a portion of the collecting aperture, however, the aperture is oversized to ensure that the 6.39m^2 collecting aperture area is achieved.

The PSF of the POEMMA optics is much less than a pixel size with an RMS diameter over the entire FoV that is no more than the 3 mm spatial pixel size of the photodetectors in the focal plane (see Figure 19). Note that this imaging requirement is nearly 10^4 away from the diffraction limit, implying optical tolerances closer to a microwave dish than an astronomical telescope are needed.

The diameter of the POEMMA primary mirror is set to fit the launch vehicle (Atlas V). The large FoV of the Schmidt photometer is required by the science capabilities. The design requires an offset between the corrector and the stop, and a slightly aspheric primary mirror (only 0.8 mm of departure from the base sphere) to achieve good image quality over the entire field of view. The specifications for the optics are listed in Table II in the Appendix. (A cross section layout is shown in Figure 18 left, spot diagrams on the 3 mm pixel scale are shown in Figure 19 right, the RMS spot size versus viewing angle in Figure 19 left, and the effective area as a function of viewing angle is in Figure 20 left.)

B. Focal Surface

The focal surface (FS) of the POEMMA photometer forms a convex spherical surface matched to the design of the optical system (Figure 18). The radius of curvature of the FS is 2.07 m. The 45° FoV of the optics leads to a FS diameter of 1.61 m. The FS is divided into

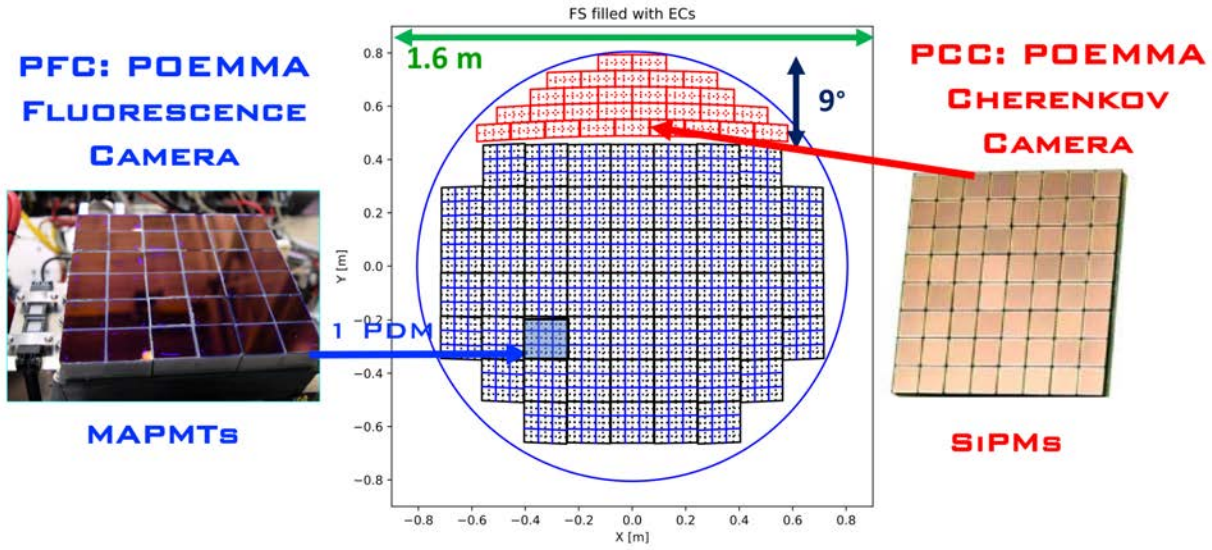

FIG. 21: Layout of the photon sensors on the focal surface. The red tiles represent the Cherenkov sensors (each tile is a FSU composed of 8 SiPMs) and the blue tiles correspond to the Fluorescence sensors (each tile is a PDM composed of 36 MAPMTs).

two sections: the POEMMA Fluorescence Camera (PFC), optimized for the fluorescence signals, and POEMMA Cherenkov Camera (PCC), optimized for for Cherenkov signals.

The PFC includes the center of the FoV and comprises 80% of the total area. The PFC records the EAS video in 1μs frames (or Gate Time Units, GTU) in the $300 \lesssim \lambda/\text{nm} \lesssim 500$ wavelength band using multi-anode photomultiplier tubes (MAPMTs). PFC sensors are from Hamamatsu (R11265-203-M64) MAPMTs with ultra-bialkali photocathodes and high quantum efficiency. Each MAPMT has 64 pixels in an 8 x 8 array. Each pixel measures 3 mm on a side and the entire MAPMT measures 30 x 30 mm^2. The MAPMTs are grouped 2 x 2 into Elementary Cells (ECs), and ECs are grouped 3 x 3 into Photon Detector Modules (PDMs), as developed for the JEM-EUSO mission [49]. The PFC is composed of 55 PDMs, as shown in Figure 21, for a total of 1,980 MAPMTs containing a total of 126,720 pixels.

Figure 20 left shows the simulation of an EAS on the PDM of a POEMMA focal surface. The signal recorded by the PFC determines the shower evolution and maximum peak, S_{max}, which is proportional to the energy of the UHECR. The stereo reconstruction of the images from both POEMMA observatories determines the geometry of the EAS and the column depth where S_{max} occurs, denoted as X_{max} (in units of g/cm^2 (see Figure 4). X_{max} is sensitive to the type of particle initiating the EAS since different particle species have different cross sections. By accurately measuring S_{max} and X_{max}, POEMMA can determine the energy and the nature of the UHECR, e.g., proton, heavier nucleus, neutrino, photon, or even exotica.

The POEMMA Cherenkov Camera uses silicon photomultipliers (SiPMs) and is optimized to observe in the $300 \lesssim \lambda/\text{nm} \lesssim 900$ wavelength band for Cherenkov emission of showers developing towards the observatory. The PCC covers 9° of the FoV extending inward from the edge on one side (see Figure 21). PCC sensors are solid-state SiPMs (Ketek PM3325-WB) assembled in arrays of 8 x 8 pixels with a total area of 31 x 31 mm^2. The SiPM units are grouped 4 x 2 into Focal Surface Units (FSUs). The tiling of 30 FSUs forms the full PCC with a total of 15,360 pixels covering the top portion of the focal surface

(Figure 21).

The PCC records EASs produced by UHECRs above the limb of the Earth and showers from τ-lepton decays below the Earth's limb induced by ν_τ interactions in the Earth.

C. Data System

The electronics and real-time software for the two sections of the focal surface (the PFC and the PCC) function independently so each can be optimized for their specific task. A single Data Processor (DP) will read out the data from both systems, store it locally and then transmit it to the S/C bus for transmission to the ground.

The search for UHECRs will be based on the PFC detection of fluorescence from EASs using the MAPMTS. An EAS will show up as a bright, persistent spot that will typically move across part of the FS depending on the viewing angle (see Figure 20 right). Each PDM will contain one SPACIROC ASIC for each MAPMT, and one PDM FPGA to search for persistence. The ASIC counts photoelectrons for each MAPMT anode individually during a 1μs GTU. The FPGA will search those counts for a persistent signal in excess of the background. The threshold for the brightness and duration of the persistent signal will be adjusted to yield a rate of no more than 7 Hz in total across the whole MAPMT system. When persistence is detected all the data will be passed to a Cluster Control Board (CCB) that will implement a search for contiguous tracks. The threshold for defining a track will be adjusted so that the total rate is no more than 0.1 Hz. When a track is detected the DP will begin the readout process.

In parallel the search for neutrinos will be based on the PCC detection of brighter but much shorter-duration Cherenkov flashes (10-100 ns) using the SiPM FSU ASICs and FPGA. Threshold cuts on the number of photo-electrons per SiPM pixel will be used to reduce the background rate due to airglow and other sources.

Upon receipt of a trigger, the DP will read out data and store it locally, eventually transferring it to the S/C bus that handles transmission to the ground stations. The DP will also handle housekeeping functions, interfaces to various auxiliary systems (e.g., infra-red cameras), and exchange of commands and data with the S/C bus.

D. Atmospheric Monitoring System

The Atmospheric Monitoring System (AMS) uses two infra-red (IR) cameras on each POEMMA observatory. These cameras will observe clouds in the 45° FoV of the main instrument [116–118]. The IR images collected through an 8 μm filter on one camera and a 11 μm filter on the other camera will be analyzed to estimate cloud top heights [119].

The IR cameras will be housed in a small enclosure mounted at the center of the corrector lens assembly, which is a blind spot caused by the focal surface, and behind the shutter (see Figure 1). Power and data will be delivered through cabling connected to the main electronics box. The camera system will use internal controllers to maintain a stable temperature within 1°C of its operating range of -40°C to 55°C. The IR camera assembly will include an integrated calibration target that can be moved in front of the camera lenses. Both cameras will take one image per minute, which is an interval based on the instrument FoV and the speed of the satellites. Each picture has a resolution of 640 by 480 pixels with 16 bits per pixel. The uncompressed picture size is 615 kB.

E. Calibration Systems

The POEMMA on-board calibration system will feature pulsed light emitting diodes (LEDs) that periodically illuminate the focal surface of the instrument. The data recorded will be used to monitor the relative photometric calibration of the instrument throughout the mission, following the methods proposed for the JEM-EUSO mission [116]. The LED system on each satellite will include 3 LED modules and one control unit. The LED modules will be mounted on the bottom side of the corrector plate holding frame. Each module contains five LEDs (340, 360, 390, 500 and 660 nm) mounted behind an opal diffuser. Power and control cables connect the LED module to the main electronics box behind the mirror. During data taking operations, the 500 nm and 360 nm LEDs will be flashed typically once per orbit. The other LEDs will be flashed during portions of the orbit when the moonlight background is too high and science data acquisition operations are suspended.

F. Power

The power system (28v) is designed for a 5-year mission, which includes the 3-year primary mission and a 2-year extended mission. It uses 7.8 m^2 of triple-junction GaAs solar cells mounted on rigid honeycomb structure to produce 2,428 W (2,050 W) at the start (end-of-life) that meets the mission demand of 2,030 W including 30% contingency. A 3-axis drive is used to maximize the solar array exposure without relying on the spacecraft attitude control system.

The energy generated by the solar array is stored in a 145 AH lithium-ion battery to provide power when the spacecraft are not in sunlight and for 60 minutes during the launch operations. This battery is designed for 27,639 charge-discharge cycles to about 20% depth of discharge in each cycle.

This power system design is based on high TRL (≥ 7) components and devices with flight heritage. The design can comfortably generate enough power to meet the needs of the Photometer and Spacecraft (see Table I for power with contingencies for each unit). It includes redundancy for critical elements to meet Class B mission requirements.

G. Mechanical Structure

The instrument structural concept was reviewed by MSFC engineering staff. The most challenging parts of the mechanical system are the deployment of the large optical elements, corrector plate and focal surface, light-shield, and the mechanical shutter. Structural analysis of the conceptual design shows a first fundamental frequency after deployment at 7.9 Hz, 60% above the IDL goal of 5 Hz, which is appropriate for such a large structure. An analysis of the stowed configuration during launch could not be completed due to the lack of design details of the launch vehicle at this stage of the design. Engineering solutions are available to meet the 15 Hz guideline through additional design effort during the instrument preliminary design phase.

The deployment of the focal surface and corrector plate rely on one-time operations of actuators that drive the folded struts to reach full extension and then lock them into place for the duration of the mission. No further adjustment of the optical system is required

due to the sizable tolerances afforded by the coarse EAS imaging requirements (which is 10^4 away from the diffraction limit).

The operation of the shutter will be critical over the duration of the mission. The shutter design is a motor driven gear system with redundant motors and gear boxes for each half of the shutter. The shutter doors are composed of light-weight honey comb structures. The shutter will protect the optical system during daytime portions of the orbit and, together with other mitigation strategies, will reduce the fluence of atomic oxygen (AO) impinging on the corrector plate during the mission. The large area of the shutter surfaces will also function as part of the thermal sub-system in maintaining a controlled environment.

H. Light shield

To prevent stray light from entering the POEMMA instrument, provide micrometeoroid protection and thermal control, a collapsible shroud will surround the optics (Figure 17). This shroud will consist of a set of three nested cylinders. Each cylinder will have Beta cloth on the outer surface and black Kapton on the inner surface. Multi-layer insulation can be added between the inner and outer surfaces, if needed. When POEMMA is stowed for launch, the nest of cylinders will be collapsed and secured. The bottom of the outer cylinder will be attached to the periphery of the mirror and the top of the inner cylinder will be attached to the aperture doorframe. The top of the outer cylinder, the bottom of the inner cylinder and both the top and bottom of the middle cylinder will have locator pins that engage holes in the periphery of the mirror and the doorframe respectively to secure them during launch. As POEMMA deploys, these pins will disengage. Cables (stowed in tubes at launch) will deploy and pull the middle cylinder into position. Rolling Kapton light baffles between the cylinders will insure that the shroud is light tight when deployed.

I. Thermal

The thermal sub-system developed during the IDL meets the requirements that are driven by the temperature range, gradient, and stability requirements for the focal surface. A thermal model was developed and the results predicted for the mission fall within the specified tolerances for key systems. Active cooling is not required based on the IDL analysis, e.g., the light shield acts as an efficient thermal radiator and the temperature control is adequate for the SiPM system.

Since significant changes were made after the IDL design, a new thermal analysis of the de-scoped system should be performed during an early phase of the preliminary design.

J. Spacecraft bus

The spacecraft (S/C) bus (Figure 22) is the hexagonal cylinder 1.55 m tall with an outside diameter of 3.37 m weighing 1,073 kg (including a 25% contingency). Located behind the POEMMA mirror (see Figure 17), it provides basic services to the observatory including on-orbit deployment, power, communications, attitude control, propulsion and avionics.

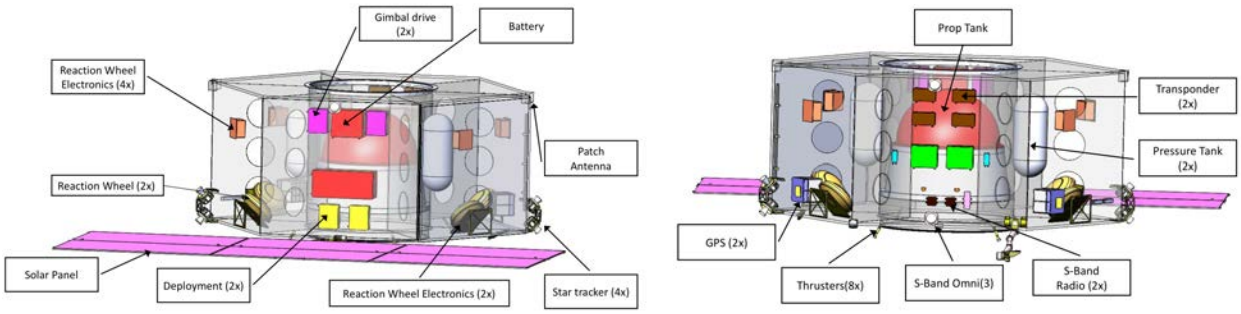

FIG. 22: Spacecraft bus MDL design with some components highlighted.

The avionics includes the command and data handling system (including the flight computer), the spacecraft clock that provides the precise timing we need for synchronization between the satellites, the gimbal drive electronics to steer the solar panels, and the control functions for all the deployment mechanisms to unfold the instrument once it reaches orbit.

1. *Communications Links*

The data volume is 7.96 Gbits/day (7.22 Gbits/day is science data, the remainder is spacecraft, housekeeping and contingency). The latency of data reaching the ground can be up to 24 hours. The satellites have onboard storage for up to 7 days of data.

Each satellite carries three S-band omni antennas. The S-band downlink requires 16 minutes of ground station contact per day, 125 minutes per day is available. Commands are normally uplinked during passes over ground stations, but the satellites also include the capability to receive ToO alerts and emergency commands linked via TDRSS through the S-band antennas.

2. *Avionics*

The avionics in each satellite consists of a prime and redundant command and data handling system based on a Rad 750 Processor with 25 GB of Memory Storage. A 100 Mhz Hz Oven-controlled crystal oscillators provide an accurate clock. It controls all the satellite functions, command and control of the science instrument, storage and transmission of the data, and reception of commands.

K. Integration and Tests

The POEMMA instrument integration will occur at a prime contractor to be selected. The integration of the instrument with the spacecraft bus and payload tests can occur at GSFC. The timeline for integration and testing, developed at the MDL, is shown in Figure 23.

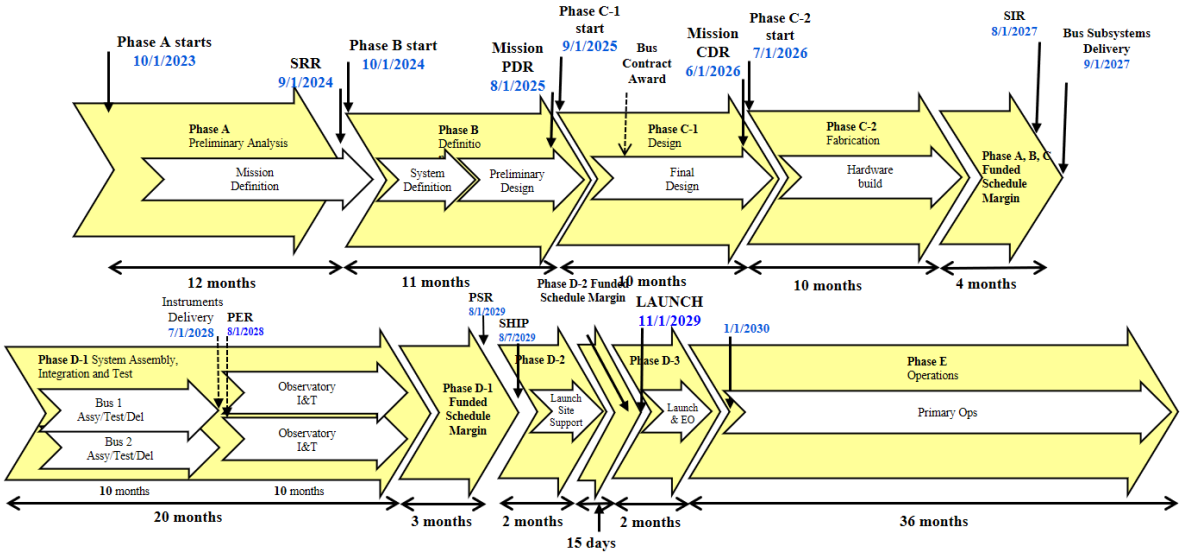

FIG. 23: Development time line.

IV. POEMMA MISSION CONCEPT

The POEMMA mission concept results from an intense work session at the Mission Design Laboratory (MDL) at the GSFC Integrated Design Center from October 30 to November 3, 2017. POEMMA is a Class B mission consisting of two identical observatories carried on identical satellites. These satellites will fly in formation observing the similar volumes of the Earth's atmosphere (Figure 2). The tandem observations allow event reconstruction of both fluorescence and Cherenkov signals using spatial and temporal coincidence (or time-delay) between the satellites.

The timeline for the mission is shown in Figure 24. The prime mission has three phases, modes 1, 2, and 3. Following on-orbit checkout, the two satellites will be oriented to point their instruments toward the zenith and separated by 300 km to calibrate them by making simultaneous observation of stars with well-known apparent luminosities (mode 1 in Figure 24). In the second phase, the instruments will be pointed close to the nadir in order to make stereo observations of the fluorescent light from cosmic ray extensive air showers (EASs) at the lowest energies (mode 2 in Figure 24 and Figure 2 right). Once sufficient statistics have been acquired at the lowest energies, the satellites separation will be reduced to 25 to 30 km and the instruments will be pointed just above the horizon to observe UHECR via Cherenkov just above the limb (mode 3 in Figure 24 and Figure 2 left). During operations in modes 2 and 3, the instruments will be re-oriented towards target of opportunity directions (ToO) when extreme luminosity photon or gravitational wave events are detected. The ToO mode will be optimized to follow the rising and setting of the transient event. During a ToO follow-up mode, measurements of fluorescence from EASs will continue utilizing the larger volumes of the atmosphere observed from the satellites to the limb. The extended mission can operate in either mode 2 or 3 depending on the science achievements of the primary mission.

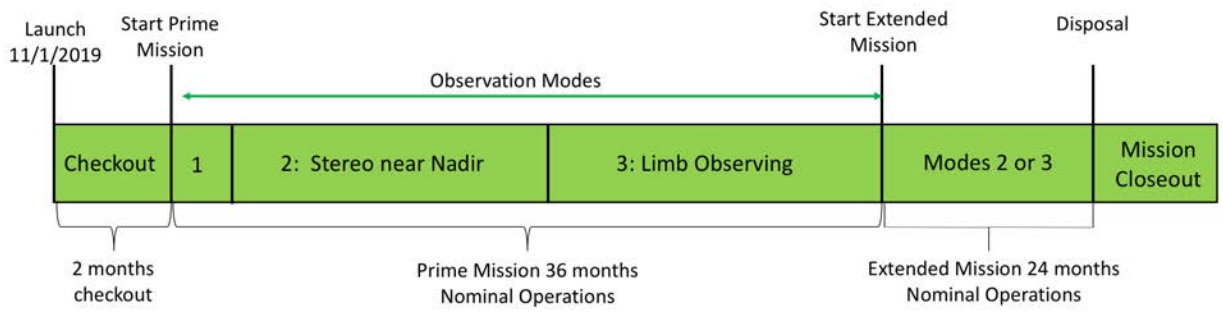

FIG. 24: Mission time line (diagram not to scale).

A. Launch Operations

The POEMMA satellites will be dual-manifested on an Atlas V using the long payload fairing as shown in Figure 25. The satellites will be launched into circular orbits at an inclination of 28.5 degrees and an altitude of 525 km, where they will remain until de-orbited for disposal in the eastern south Pacific at the end of the mission.

The satellites are launched in a stowed configuration. Once on orbit, the corrector plate and focal surface will be deployed into their final position. As the instruments deploy, a telescoping shroud surrounding the optical bench will deploy, keeping the instrument light-tight while providing micrometeoroid protection and thermal control. A solar array will be deployed from each spacecraft bus (that are located behind the mirrors). These arrays are three-axis gimballed and track the sun.

B. On-Orbit Operations

POEMMA makes observations in umbra and in low moonlight conditions. The satellites will orbit the Earth with a period of 95 minutes, orbiting the Earth ~15 times per day. As the satellites are leaving umbra the aperture doors are closed to protect the focal surface. They are opened again as the satellites are entering umbra during each orbit, up to 30 door operations per day. When the aperture doors are open, the satellites are oriented so that the optical axis is over 90° away from the RAM direction. During observations the attitude of the satellites must be maintained within 0.1° with knowledge of the attitude to within 0.01°. Events will be time-tagged with a relative accuracy within 25 ns between the satellites.

In case the mission operators loose attitude control of one or both POEMMA satellites, the satellites will automatically go into safe mode and the aperture doors will be closed to prevent sunlight exposure and atomic oxygen damage to the Schmidt corrector's exterior surface.

The satellites are maneuvered on orbit by means of four reaction wheels (unloaded with torque rods) for attitude control and changes of attitude. The satellites also have eight hydrazine thrusters each that are used for changing their orbital separation and for de-orbiting at the end of the mission. In addition to changes in separation between the early phases of the mission, these thrusters are used to maintain accurate satellite separations during phase 4 of the mission to tighten the temporal coincidence window

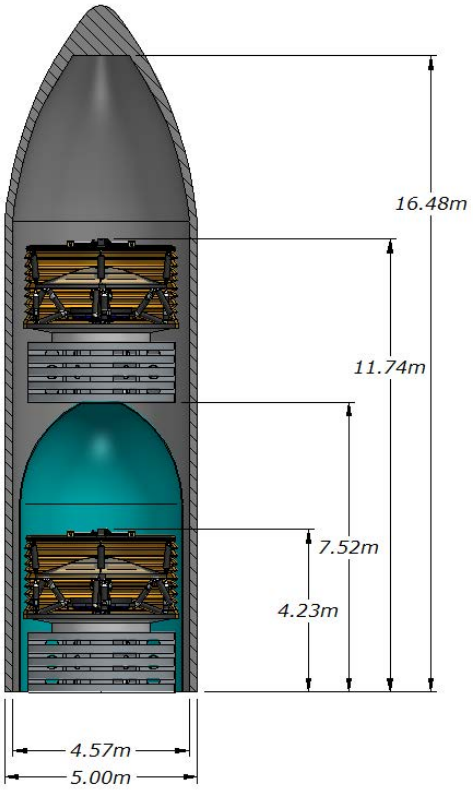

FIG. 25: Dual Launch Manifest in Atlas V.

between the satellites to 25 ns. The satellites have star trackers, sun sensors for accurate attitude knowledge.

The mission control center for POEMMA will be GSFC and the Science Operations Center will be at the University of Chicago.

V. POEMMA COST

We estimate POEMMAs total life cycle cost between $ 0.936 and $ 1.048 billion in FY18 dollars, including reserves and the launch vehicle according to the ground rules of the NASA probe study. The table in Figure 26 shows the high level overview of three bounding cost estimates. The Study Team (ST) estimate is based on the Goddard Space Flight Center (GSFC) Integrated Design Lab (IDC) parametric cost model of the first iteration of the mission concept. This concept was costed to be well over the $1B Probe-class limit and was de-scoped to the concept presented in our report. The ST estimate preserved individual component, subsystem, structure, integration/test, labor and ground support costs from the IDC model and scaled them in a conservative manner appropriate to the de-scoped concept in order to arrive at the total mission lifecycle cost.

In addition to the ST estimate, two more parametric cost models were constructed by the Engineering Cost Office (ECO) at Marshall Space Flight Center (MSFC). One used the TruePlanning R software from PRICE Systems, LLC for the payload/instrument and the

Cost Element	PCEC/PRICE (MSFC)	PCEC/SEER (MSFC)	Study Team (ST) (Based on IDC)	Comments
1. Project Management	23.57	23.57	38.90	
2. Systems Engineering	18.76	18.76	38.90	
3. Safety & Mission Assurance	14.64	14.64	26.8	
4. Science/Technology	18.73	18.73	48.70	
5. Payload / Instrument (2)	274.06	284.92	317.50	
6. Flight System / Spacecraft (2)	194.33	194.33	217.80	
7. Mission Operations	40.92	40.92	7.70	
8. Launch Vehicle	150.00	150.00	150.00	Study ground rules
9. Ground Data System	-	-	11.70	
10. System Integration & Test	14.36	14.36	27.5	
11. Education & Public Outreach	-	-	-	
Reserves (25% for MSFC est.)	187.34	190.06	170.00	170 mandated by HQ
Total (M$ FY18)	**936.71**	**950.29**	**1055.50**	

FIG. 26: High level cost overview. Amounts in millions of FY18 dollars.

NASA Project Cost Estimate Capability (PCEC) system for the spacecraft. The second model used the SEER for Hardware, Electronics & Systems cost estimation software from Galorath, Inc. for the payload/instrument and PCEC for the spacecraft. Assumptions common to these estimates were for a Class B mission, 4-6 year development schedule, launch in the 2027-2029 time frame and $150M for launch services. Reserves were set by NASA Headquarters (HQ) to be $170M. However, the MSFC ECO typically sets reserves to 25% at minimum. The MSFC ECO cost models were constructed at the subsystem level utilizing the Master Equipment List (MEL) from the GSFC IDC Instrument Design Lab (IDL) for the payload/instrument adjusted by the Study Team as required by the concept de-scope, and the MEL from the GSFC IDC Mission Design Lab (MDL) for the spacecraft. The three total costs represent point estimates and have not explored sensitivities to mass and schedule. The IDL run was conducted in July 2017, the MDL run in October 2017 and the MSFC ECO study in January-February 2018.

The single largest driver of the overall cost is the instrument primary mirror and corrector plate (lens) optical assemblies. The first iteration of the mission concept sported a petal-deployed segmented primary mirror of 6 meter diameter, and was the chief cause of the total mission cost exceeding the $1B limit in the IDC study. The de-scoped concept detailed in our report sees the primary mirror diameter and complexity greatly reduced, presently a 4 meter monolithic structure. Even a mirror of this size has heretofore never been operated in space. However, it is important to emphasize that prior **large space-based optical telescopes are highly inappropriate reference points for cost prediction** in this case. POEMMA requires nothing like the angular resolution capability of Hubble, JWST or even early gamma-ray telescopes. Figure and surface tolerance requirements for the POEMMA primary mirror and corrector plate are so low that the instrument can be considered merely a 'photon bucket'. For example, existing space-based telescopes for UV-Vis-IR astronomy require primary mirror surface precision in the range of 10-100 nanometer RMS, whereas POEMMA only requires approximately 0.5 millimeter RMS, 4-5 orders of magnitude lower, i.e., more comparable to a radio or communications antenna (see Figure 27). This has a dramatic effect on development cost. Rather than gold-coated

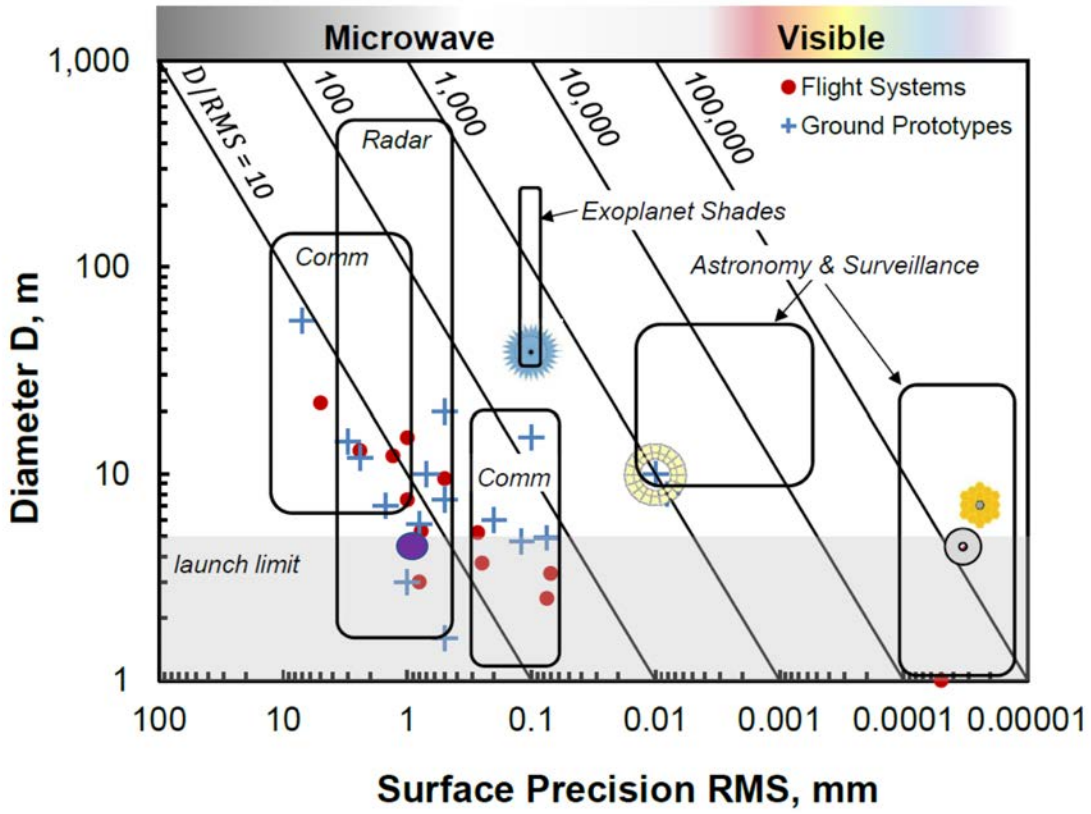

FIG. 27: Primary mirror diameter vs RMS surface precision for historical missions. POEMMA (in purple) falls at or below the D/RMS=10 contour. Hubble and the JWST have D/RMS > 100,000 [120].

honey-combed beryllium or ultra-low expansion glass, the POEMMA primary mirror can be fabricated out of metallic-coated carbon fiber reinforced plastic and the corrector lens out of an acrylic such as Polymethyl methacrylate (PMMA). These considerations were captured in the MSFC ECO PRICE model by choosing the Manufacturing Complexity for Structures (MCPLXS) parameter for POEMMAs optics to be rated as Excellent rather than Highest and in the SEER model the Complexity of Form and Fit parameters were set to Nominal/High rather than Very High or Extra High. In both the PRICE and SEER models, the corrector plate was classified as a Secondary Structure.

For validation of the POEMMA cost estimate, the MSFC ECO team compared their final value to total mass versus overall cost data for historical missions. The plot in Figure 28 shows the result. The cost for a single POEMMA spacecraft (green) falls on trend line model for all missions (dashed black). However, based on the reasoning above, it would be more appropriate to compare POEMMA to non-imaging missions (red dots and red-dashed line). Given the front-loaded costs for a Class B mission, the second POEMMA satellite costs significantly less than the first. The GSFC IDC and MSFC ECO results confirm that the spacecraft exact copy costs 25% of the first POEMMA satellite for Class A/B missions (blue triangle). This is a factor of two less than is customary for Class C/D missions since payload management, systems engineering, and safety/mission assurance costs are much higher for Class A/B missions and are not recurring for exact spacecraft copies. The complete POEMMA mission (magenta triangle) falls just below

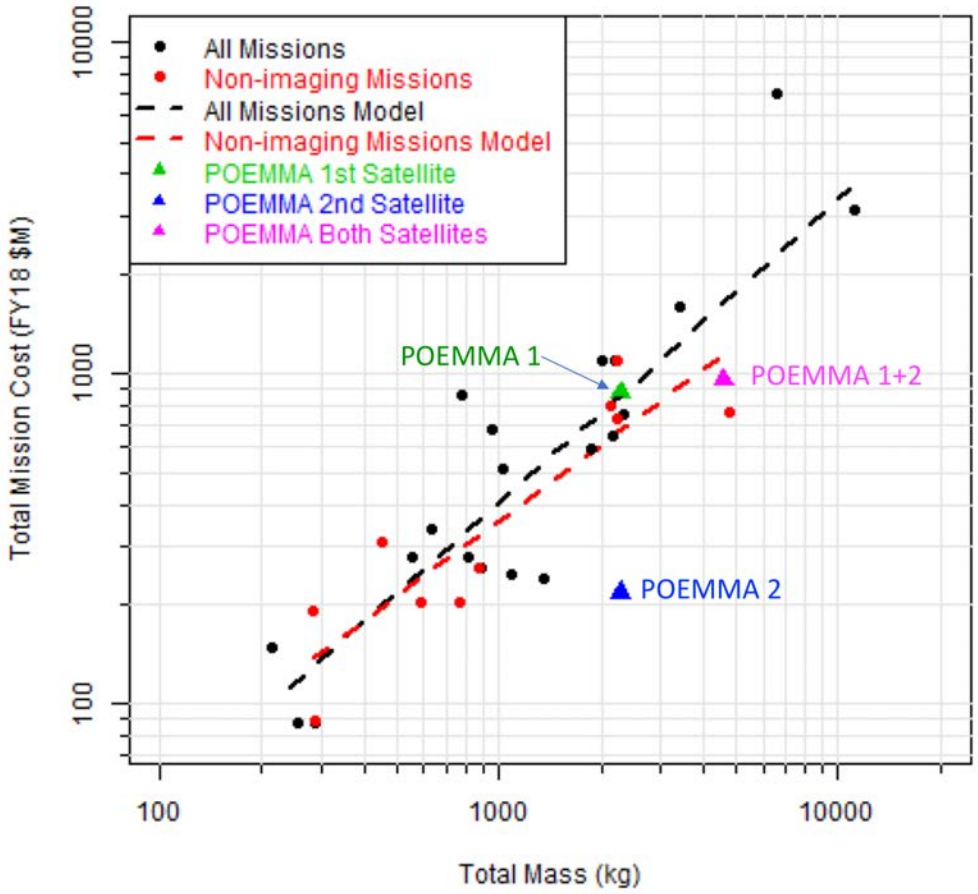

FIG. 28: POEMMA costs as compared to other space telescopes. The cost of one unit of POEMMA aligns well with historic telescope costs while the second unit adds 25% to the total cost. (Historical Missions include: ACTS, CALIPSO, Cloudsat, EO-1 / ALI, FUSE, GALEX, Herschel, HST, ICESat, IRAS, IUE, JWST, Kepler, MRO/HiRISE, OAO-2/CEP, OAO-3/PEP, OAO-B/GEP, Planck, SOHO/EIT, Spitzer, STEREO/SECCHI A, SWAS, TDRS-1, TDRS-7, TRACE, WIRE, WISE, WMAP.)

the non-imaging mission cost-vs-mass trend line model (red dashed).

VI. TECHNOLOGY ROADMAP

The POEMMA conceptual study relies primarily on simple and proven technology. No new technologies are required to be developed for the mission. However, POEMMA can take advantage of technologies as they mature. Those elements beneficial to POEMMA are listed here with a description of the desired maturation and rationale. POEMMA team members are actively working on the maturation of a number of these components through laboratory, sub-orbital (EUSO-SPB1 and EUSO-SPB2), and spaceflight (mini-EUSO) testing.

A. Mechanical

The shutter doors must operate during the entire mission and are the highest mission risk. This risk can be reduced during early phases of the project through iterative design and testing cycles. Fortunately, this sub-system is well suited for ground testing by off-loading its mass in the 1g ground environment and cycling through the operation cycle in a large thermal-vacuum (T/V) chamber. The reliability of the drive train can be tested by itself over an accelerated period in a small T/V chamber for the full number of cycles anticipated for the mission. Testing will verify the performance of the design, workmanship and motor operations reducing the likelihood of malfunctions of the shutter during the mission. Final verification can be a full up cycle test in a T/V chamber together with deployment of the focal surface, corrector plate and light shield to verify the operation of the full mechanical system.

There are engineering solutions to ensure the structural integrity of the instrument in the stowed and deployed positions will survive launch and meet observing requirements. Additional design effort is required to identify the best approach and can be addressed early in the preliminary design phase.

B. Optics

The baseline POEMMA optics meets science requirements with no issue for manufacturing. There are a number of technology advances that can increase the performance or reduce risk that can further improve the design.

Space qualified UV coatings resistant to atomic oxygen (AO) are under development for a number of projects. An appropriate coating on the POEMMA corrector plate can mitigate risks of prolonged exposure to the RAM direction. This would also enable freer selection of the ToO observations.

An advanced split mirror design (bi-focal) for the Limb observations can enhance our ability to identify Cherenkov events by splitting the image between two pixels for an internal coincidence test that further improve immunity to spurious signals that may be generated in the focal surface electronics.

A new optics design for wider FoV for limb observations is under development to improve the detection of diffuse neutrino emission versus the ToO mode.

C. Focal surface: SiPM

The two POEMMA focal surface sections, the PFC and the PCC, were studied during the IDL. The IDL study concluded that the MAPMT-based PFC section could be built today with existing technology. The PCC SiPM-based section would benefit greatly from technology development in the following areas:

1. space qualification of SiPM arrays and silicon photo-diodes that are appropriate for this application
2. packaging schemes for those arrays and diodes that allow the FSU to conform to the focal surface
3. further development and space flight qualification of the SiPM ASIC and its interface to the SiPM arrays.

Investment in the development of large-scale SiPM-based arrays for space-based applications will benefit other future missions that depend on Cherenkov detection as well as POEMMA, e.g., gamma-ray astronomy and studies of transient luminous events (TLE) in the upper atmosphere. All three of the development areas are therefore actively being studied in the laboratory and with sub-orbital testing:

1. Members of POEMMA are currently participating in a NASA Super-Pressure Balloon program (SPB) with the EUSO collaboration:

a. The first SPB flight (EUSO-SPB1) included an early prototype of a SiPM-based system. It provided extensive information about the operation of SiPM at the low temperatures and pressures of the upper atmosphere and also the background UV environment.

b. Funding for a second EUSO-SPB2 flight has now been approved as part of the APRA program. EUSO-SPB2 is specifically planned to serve as a pathfinder for POEMMA. The aim is to include a focal surface section that is tiled with SiPM arrays, which are read-out by full-functionality prototype FSUs.

2. A separate APRA proposal was submitted to NASA by members of the POEMMA collaboration specifically to develop that prototype FSU for EUSO-SPB2 and POEMMA. The proposal has been accepted and will be funded for 3 years beginning in 2019. During those 3 years:

a. The interface between SiPM arrays and ASICS will be developed and optimized for the UV environment of the upper atmosphere and Low Earth orbit.

b. That system will be tested in the laboratory at MSFC and in the field, possibly utilizing a one-day test flight scheduled for EUSO-SPB2

c. The integration of the FSU into the EUSO-SPB2 payload will begin.

D. Numerical Simulations

We have simulated many aspects of the POEMMA science, but much can be learned from end-to-end simulations of high-altitude and upward-going EASs and the associated POEMMA sensitivity. For the UHECR simulations, further development of EAS reconstruction in both the stereo and limb-viewing mode will improve the fidelity of quantifying POEMMAs performance, leading to potential improvements in UHECR EAS measurement performance. For example, including the EAS time development in the stereo reconstruction should improve stereo reconstruction efficiency, while also improving the angular and X_{max} resolution as compared to that for the pure geometrical reconstruction we have initially used. Further improvements in the modeling of the monocular performance are underway, including the improvements on the reconstruction of observed EASs using reduced time sampling. Our current modeling of the tau-lepton EAS Cherenkov signal uses a baseline end-to-end simulation. This is currently being improved under a neutrino modeling APRA-funded program that was initiated by this POEMMA work. These improvements in the fluorescence and Cherenkov signal modeling will help optimize the observing strategy including best observing angles and satellite separations.

Theoretical models of extremely energetic transient events are currently being developed by many authors given the recent capabilities in multi-messenger observations. A careful survey of the most likely neutrino emitters together with the brightest neutrino time-scales will help prioritize a sequence of ToO targets to maximize the discovery potential of POEMMA.

VII. SUMMARY

POEMMA is a unique probe-class mission designed to answer fundamental open questions in the multi-messenger domain during the next decade. Community driven white-papers on the UHECR science [41] and astrophysical neutrino science [121, 122] describe the scientific challenges that POEMMA will address. The multi-messenger domain began over the last decade and it will flourish during the 2020s with the capability provided by POEMMA.

VIII. APPENDIX I: ACRONYM LIST

AMS: Atmospheric Monitoring System
CCB: Cluster Control Board
DP: Data Processor
EAS: Extensive Air Shower
EC: Elementary Cells
EFL: Effective Focal Length
EPD: Effective Pupil Diameter
FPGA: Field Programmable Gate Array
FSU: Focal Surface Units
GSFC: Goddard Space Flight Center
GTU: Gate Time Units
IDL: Instrument Design Laboratory
IDC: Integrated Design Center
JEM-EUSO: Joint Experiment Missions for Extreme Universe Space Observatory
LED: Light Emitting Diodes
MAPMT: Multi-Anode Photo-Multiplier Tubes
MSFC: Marshall Space Flight Center
PCC: POEMMA Cherenkov Camera
PDM: Particle Detector Modules
PFC: POEMMA Fluorescence Camera
POEMMA: Probe Of Extreme Multi-Messenger Astrophysics
PSF: Point Spread Function
S/C: Spacecraft
SiPM: Silicon Photo-Multipliers
SPACIROC ASIC

IX. APPENDIX II: OPTICS SPECIFICATION

TABLE II: **Optics Specifications:**

R	= spherical base radius of curvature
k	= conic constant
A to F	= 4th to 14th rotation symmetric polynom. coeff.
Surface diameters	and relative locations (vertex distances)
Stop Diameter	= 3,300 mm
Stop to Corrector	= 889.6 mm
Corrector center thickness	= 12.25 mm
Corrector diameter	= 3,300 mm
Corrector to Mirror	= 4,032.8 mm
Mirror diameter	= 4,000 mm
Corrector to Focal Surface	= 2,105.9 mm
Focal Surface to Mirror	= 1,926.9 mm
Focal Surface diameter	= 1.61 m
Surface Form	
External Corrector Surface:	
R	=1,825.7 mm
A	= -5.97872 10^{-10}/mm^3
B	= 1.06661 10^{-15}/mm^5
C	= -9.89055 10^{-22}/mm^7
D	= 4.62547 10^{-28}/mm^9
E	= -1.07407 10^{-34}/mm^{11}
F	= 9.81265 10^{-42}/mm^{13}
Internal Corrector Surface:	
R	= 1,897.1 mm
A	= -6.01297 10^{-10}/mm^3
B	= 1.08541 10^{-15}/mm^5
C	= -1.00484 10^{-21}/mm^7
D	= 4.71169 10^{-28}/mm^9
E	= -1.09889 10^{-34}/mm^{11}
F	= 1.01227 10^{-41}/mm^{13}
Edge thickness of corrector	$\sim$ 34 mm
Mirror	
R =	3,991.7 mm
k =	1.77565 10^{-2}
Focal Surface	
R =	2,074.4 mm

[1] J. Linsley, Evidence for a Primary Cosmic-Ray Particle with Energy 10^{20} eV, Phys. Rev. Lett. **10**, 146 (1963)

[2] G. L. Cassiday, Observatory for Ultra High-Energy Processes: The Fly's Eye, Annual Review of Nuclear and Particle Science Vol. 35:321-349 (1985)

[3] M. Takeda et al., Phys. Rev. Lett. 81, 1163 (1998)

[4] G. Thomson et al., Nucl. Phys. B 36, 28 (2004)

[5] J. Abraham *et al.* [Pierre Auger Collaboration], Trigger and aperture of the surface detector array of the Pierre Auger Observatory, Nucl. Instrum. Meth. A **613**, 29 (2010).

[6] J. A. Abraham *et al.* [Pierre Auger Collaboration], The fluorescence detector of the Pierre Auger Observatory, Nucl. Instrum. Meth. A **620**, 227 (2010) [arXiv:0907.4282].

[7] A. Aab *et al.* [Pierre Auger Collaboration], The Pierre Auger Observatory: Contributions to the 35th International Cosmic Ray Conference (ICRC 2017), arXiv:1708.06592 [astro-ph.HE].

[8] T. Abu-Zayyad *et al.* [Telescope Array Collaboration], The surface detector array of the Telescope Array experiment, Nucl. Instrum. Meth. A **689**, 87 (2013) doi:10.1016/j.nima.2012.05.079 [arXiv:1201.4964 [astro-ph.IM]].

[9] H. Tokuno *et al.*, New air fluorescence detectors employed in the Telescope Array experiment, Nucl. Instrum. Meth. A **676**, 54 (2012) doi:10.1016/j.nima.2012.02.044 [arXiv:1201.0002 [astro-ph.IM]].

[10] K. Kotera and A. V. Olinto, The astrophysics of ultrahigh energy cosmic rays, Ann. Rev. Astron. Astrophys. **49**, 119 (2011) doi:10.1146/annurev-astro-081710-102620 [arXiv:1101.4256 [astro-ph.HE]].

[11] L. A. Anchordoqui, Ultra-high-energy cosmic rays, arXiv:1807.09645 [astro-ph.HE].

[12] R. A. Batista et al., Open Questions in Cosmic-Ray Research at Ultrahigh Energies Frontiers in Astronomy and Space Sciences 2019.

[13] P. Blasi, R. I. Epstein and A. V. Olinto, Ultrahigh-energy cosmic rays from young neutron star winds, Astrophys. J. **533**, L123 (2000) doi:10.1086/312626 [astro-ph/9912240].

[14] K. Fang, K. Kotera and A. V. Olinto, Newly-born pulsars as sources of ultrahigh energy cosmic rays, Astrophys. J. **750**, 118 (2012) doi:10.1088/0004-637X/750/2/118 [arXiv:1201.5197 [astro-ph.HE]].

[15] K. Fang, K. Kotera and A. V. Olinto, Ultrahigh energy cosmic ray nuclei from extragalactic pulsars and the effect of their Galactic counterparts, JCAP **1303**, 010 (2013) doi:10.1088/1475-7516/2013/03/010 [arXiv:1302.4482 [astro-ph.HE]].

[16] P. L. Biermann and P. A. Strittmatter, Synchrotron emission from shock waves in active galactic nuclei, Astrophys. J. **322**, 643 (1987). doi:10.1086/165759

[17] J. P. Rachen and P. L. Biermann, Extragalactic ultrahigh-energy cosmic rays 1: Contribution from hot spots in FR-II radio galaxies, Astron. Astrophys. **272**, 161 (1993) [astro-ph/9301010].

[18] B. Eichmann, J. P. Rachen, L. Merten, A. van Vliet and J. Becker Tjus, Ultra-high-energy cosmic rays from radio galaxies, JCAP **1802**, no. 02, 036 (2018) doi:10.1088/1475-7516/2018/02/036 [arXiv:1701.06792 [astro-ph.HE]].

[19] L. A. Anchordoqui, G. E. Romero and J. A. Combi, Heavy nuclei at the end of the cosmic ray spectrum?, Phys. Rev. D **60**, 103001 (1999) doi:10.1103/PhysRevD.60.103001 [astro-ph/9903145].

[20] L. A. Anchordoqui, Acceleration of ultrahigh-energy cosmic rays in starburst superwinds,

Phys. Rev. D **97**, no. 6, 063010 (2018) doi:10.1103/PhysRevD.97.063010 [arXiv:1801.07170 [astro-ph.HE]].
[21] E. Waxman, Cosmological gamma-ray bursts and the highest energy cosmic rays, Phys. Rev. Lett. **75**, 386 (1995) doi:10.1103/PhysRevLett.75.386 [astro-ph/9505082].
[22] M. Vietri, On the acceleration of ultrahigh-energy cosmic rays in gamma-ray bursts, Astrophys. J. **453**, 883 (1995) doi:10.1086/176448 [astro-ph/9506081].
[23] A. Aab *et al.* [Pierre Auger Collaboration], The Pierre Auger Observatory Upgrade - Preliminary Design Report, arXiv:1604.03637 [astro-ph.IM].
[24] E. Kido [Telescope Array Collaboration], The TAx4 experiment, PoS ICRC **2017**, 386 (2018). doi:10.22323/1.301.0386
[25] R. U. Abbasi *et al.* [HiRes Collaboration], First observation of the Greisen-Zatsepin-Kuzmin suppression, Phys. Rev. Lett. **100**, 101101 (2008) doi:10.1103/PhysRevLett.100.101101 [astro-ph/0703099].
[26] J. Abraham *et al.* [Pierre Auger Collaboration], Observation of the suppression of the flux of cosmic rays above 4×10^{19} eV, Phys. Rev. Lett. **101**, 061101 (2008) doi:10.1103/PhysRevLett.101.061101 [arXiv:0806.4302 [astro-ph]].
[27] J. Abraham *et al.* [Pierre Auger Collaboration], Measurement of the energy spectrum of cosmic rays above 10^{18} eV using the Pierre Auger Observatory, Phys. Lett. B **685**, 239 (2010) doi:10.1016/j.physletb.2010.02.013 [arXiv:1002.1975 [astro-ph.HE]].
[28] T. Abu-Zayyad *et al.* [Telescope Array Collaboration], The cosmic ray energy spectrum observed with the surface detector of the Telescope Array experiment, Astrophys. J. **768**, L1 (2013) doi:10.1088/2041-8205/768/1/L1 [arXiv:1205.5067 [astro-ph.HE]].
[29] K. Greisen, End to the cosmic ray spectrum?, Phys. Rev. Lett. **16**, 748 (1966) doi:10.1103/PhysRevLett.16.748.
[30] G. T. Zatsepin and V. A. Kuzmin, Upper limit of the spectrum of cosmic rays, JETP Lett. **4**, 78 (1966) [Pisma Zh. Eksp. Teor. Fiz. **4**, 114 (1966)].
[31] D. Allard, *et al.* Implications of the cosmic ray spectrum for the mass composition at the highest energies, JCAP 0810, 033 (2008) [arXiv:0805.4779 [astro-ph]]
[32] M. S. Pshirkov, P. G. Tinyakov and F. R. Urban, New limits on extragalactic magnetic fields from rotation measures, Phys. Rev. Lett. **116**, no. 19, 191302 (2016) doi:10.1103/PhysRevLett.116.191302 [arXiv:1504.06546 [astro-ph.CO]].
[33] E. Waxman and J. Miralda-Escude, Images of bursting sources of high-energy cosmic rays I: Effects of magnetic fields, Astrophys. J. **472**, L89 (1996) doi:10.1086/310367 [astro-ph/9607059].
[34] G. R. Farrar, R. Jansson, I. J. Feain and B. M. Gaensler, Galactic magnetic deflections and Centaurus A as a UHECR source, JCAP **1301**, 023 (2013) doi:10.1088/1475-7516/2013/01/023 [arXiv:1211.7086 [astro-ph.HE]].
[35] G. R. Farrar and M. S. Sutherland, Deflections of UHECRs in the Galactic magnetic field, arXiv:1711.02730 [astro-ph.HE].
[36] A. Aab *et al.* [Pierre Auger Collaboration], Observation of a large-scale anisotropy in the arrival directions of cosmic rays above 8×10^{18} eV, Science **357**, no. 6537, 1266 (2017) doi:10.1126/science.aan4338 [arXiv:1709.07321 [astro-ph.HE]].
[37] R. U. Abbasi *et al.* [Telescope Array Collaboration], Indications of intermediate-scale anisotropy of cosmic rays with energy greater than 57 EeV in the Northern sky measured with the surface detector of the Telescope Array experiment, Astrophys. J. **790**, L21 (2014) doi:10.1088/2041-8205/790/2/L21 [arXiv:1404.5890 [astro-ph.HE]].

[38] K. Kawata *et al.* [Telescope Array Collaboration], Ultra-high-energy cosmic-ray hotspot observed with the Telescope Array surface detectors, PoS ICRC **2015**, 276 (2016).
[39] A. Aab *et al.* [Pierre Auger Collaboration], An Indication of anisotropy in arrival directions of ultra-high-energy cosmic rays through comparison to the flux pattern of extragalactic gamma-ray sources, Astrophys. J. **853**, no. 2, L29 (2018) doi:10.3847/2041-8213/aaa66d [arXiv:1801.06160 [astro-ph.HE]].
[40] J. Biteau *et al.* [Telescope Array and Pierre Auger Collaborations], Covering the sphere at ultra-high energies: full-sky cosmic-ray maps beyond the ankle and the flux suppression, To be published in Proceedings of Ultra High Energy Cosmic Rays 2018, 8 - 12 October 2018, Paris.
[41] F. Sarazin et al., What is the Nature and Origin of the Highest-Energy Particles in the Universe?, white paper for the 2020 Decadal Survey, 2019
[42] R. Engel and J. Oehlschläger, private communication
[43] W. Bietenholz in arXiv:1305.1346
[44] M. Tanabashi et al. [Particle Data Group], Review of Particle Physics, Phys. Rev. D 98, no. 3, 030001 (2018). doi:10.1103/PhysRevD.98.030001
[45] M. Ave *et al.* [AIRFLY Collaboration], Measurement of the pressure dependence of air fluorescence emission induced by electrons, Astropart. Phys. **28**, 41 (2007) doi:10.1016/j.astropartphys.2007.04.006 [astro-ph/0703132 [ASTRO-PH]].
[46] J. Krizmanic, D. Bergman and P. Sokolsky, The modeling of the nuclear composition measurement performance of the Non-Imaging CHErenkov Array (NICHE), arXiv:1307.3918 [astro-ph.IM].
[47] R. C. d. Anjos, J. F. Soriano, L. A. Anchordoqui, T. C. Paul, D. F. Torres, J. F. Krizmanic, T. A. D. Paglione, R. J. Moncada, F. Sarazin, L. Wiencke, and A. V. Olinto, Ultrahigh-energy cosmic ray composition from the distribution of arrival directions, Phys. Rev. D **98**, 123018 (2018) doi:10.1103/PhysRevD.98.123018 [arXiv:1810.04251 [astro-ph.HE]].
[48] C. Guépin, F. Sarazin, J. Krizmanic, J. Loerincs, A. Olinto, and A. Piccone, Geometrical Constraints of Observing Very High Energy Earth-Skimming Neutrinos from Space, [arXiv:1812.07596 [astro-ph.IM]]
[49] J. H. Adams *et al.* [JEM-EUSO Collaboration], An evaluation of the exposure in nadir observation of the JEM-EUSO mission, Astropart. Phys. **44**, 76 (2013) doi:10.1016/j.astropartphys.2013.01.008 [arXiv:1305.2478 [astro-ph.HE]].
[50] A. Neronov, D. V. Semikoz, I. Vovk and R. Mirzoyan, Cosmic-ray composition measurements and cosmic ray background-free γ-ray observations with Cherenkov telescopes, Phys. Rev. D **94**, no. 12, 123018 (2016) doi:10.1103/PhysRevD.94.123018 [arXiv:1610.01794 [astro-ph.IM]].
[51] K. Fang and B. D. Metzger, High-Energy Neutrinos from Millisecond Magnetars formed from the Merger of Binary Neutron Stars, Astrophys. J. **849**, no. 2, 153 (2017) [Astrophys. J. **849**, 153 (2017)] doi:10.3847/1538-4357/aa8b6a [arXiv:1707.04263 [astro-ph.HE]].
[52] S. S. Kimura, K. Murase, P. Mszros and K. Kiuchi, High-Energy Neutrino Emission from Short Gamma-Ray Bursts: Prospects for Coincident Detection with Gravitational Waves, Astrophys. J. **848**, no. 1, L4 (2017) doi:10.3847/2041-8213/aa8d14 [arXiv:1708.07075 [astro-ph.HE]].
[53] K. Fang, B. D. Metzger, K. Murase, I. Bartos and K. Kotera, Multimessenger Implications of AT2018cow: High-Energy Cosmic Ray and Neutrino Emissions from Magnetar-Powered Super-Luminous Transients, arXiv:1812.11673 [astro-ph.HE].
[54] M. G. Aartsen *et al.* [IceCube Collaboration], Neutrino emission from the direction of the

blazar TXS 0506+056 prior to the IceCube-170922A alert, Science **361**, no. 6398, 147 (2018). doi:10.1126/science.aat2890 [arXiv:1807.08794 [astro-ph.HE]].
[55] M. H. Reno, T. M. Venters, J. F. Krizmanic, C. Guépin, A. V. Olinto and L. A. Anchordoqui, Target-of-opportunity detection of cosmic tau neutrinos from bright astrophysical transients, in preparation.
[56] J. G. Learned and S. Pakvasa, Detecting tau-neutrino oscillations at PeV energies, Astropart. Phys. **3**, 267 (1995) doi:10.1016/0927-6505(94)00043-3 [hep-ph/9405296, hep-ph/9408296].
[57] V. S. Berezinsky and G. T. Zatsepin, Cosmic rays at ultrahigh-energies (neutrino?), Phys. Lett. **28B**, 423 (1969). doi:10.1016/0370-2693(69)90341-4
[58] F. W. Stecker, Diffuse fluxes of cosmic high-energy neutrinos, Astrophys. J. **228**, 919 (1979). doi:10.1086/156919
[59] C. T. Hill and D. N. Schramm, Ultra-high-energy cosmic ray neutrinos, Phys. Lett. B **131**, 247 (1983) [Phys. Lett. **131B**, 247 (1983)]. doi:10.1016/0370-2693(83)91130-9
[60] R. Engel, D. Seckel and T. Stanev, Neutrinos from propagation of ultrahigh-energy protons, Phys. Rev. D **64**, 093010 (2001) doi:10.1103/PhysRevD.64.093010 [astro-ph/0101216].
[61] Z. Fodor, S. D. Katz, A. Ringwald and H. Tu, Bounds on the cosmogenic neutrino flux, JCAP **0311**, 015 (2003) doi:10.1088/1475-7516/2003/11/015 [hep-ph/0309171].
[62] M. Ave, N. Busca, A. V. Olinto, A. A. Watson and T. Yamamoto, Cosmogenic neutrinos from ultra-high energy nuclei, Astropart. Phys. **23**, 19 (2005) doi:10.1016/j.astropartphys.2004.11.001 [astro-ph/0409316].
[63] D. Hooper, A. Taylor and S. Sarkar, The Impact of heavy nuclei on the cosmogenic neutrino flux, Astropart. Phys. **23**, 11 (2005) doi:10.1016/j.astropartphys.2004.11.002 [astro-ph/0407618].
[64] L. A. Anchordoqui, H. Goldberg, D. Hooper, S. Sarkar and A. M. Taylor, Predictions for the cosmogenic neutrino flux in light of new data from the Pierre Auger Observatory, Phys. Rev. D **76**, 123008 (2007) doi:10.1103/PhysRevD.76.123008 [arXiv:0709.0734 [astro-ph]].
[65] M. Ahlers, L. A. Anchordoqui, M. C. Gonzalez-Garcia, F. Halzen and S. Sarkar, GZK neutrinos after the Fermi-LAT diffuse photon flux measurement, Astropart. Phys. **34**, 106 (2010) doi:10.1016/j.astropartphys.2010.06.003 [arXiv:1005.2620 [astro-ph.HE]].
[66] K. Kotera, D. Allard and A. V. Olinto, Cosmogenic neutrinos: parameter space and detectabilty from PeV to ZeV, JCAP **1010**, 013 (2010) doi:10.1088/1475-7516/2010/10/013 [arXiv:1009.1382 [astro-ph.HE]].
[67] M. Ahlers and F. Halzen, Minimal cosmogenic neutrinos, Phys. Rev. D **86**, 083010 (2012) doi:10.1103/PhysRevD.86.083010 [arXiv:1208.4181 [astro-ph.HE]].
[68] R. Alves Batista, R. M. de Almeida, B. Lago and K. Kotera, Cosmogenic photon and neutrino fluxes in the Auger era, arXiv:1806.10879 [astro-ph.HE].
[69] M. Ahlers, L. A. Anchordoqui and S. Sarkar, Neutrino diagnostics of ultra-high energy cosmic ray protons, Phys. Rev. D **79**, 083009 (2009) doi:10.1103/PhysRevD.79.083009 [arXiv:0902.3993 [astro-ph.HE]].
[70] M. G. Aartsen *et al.* [IceCube Collaboration], Differential limit on the extremely-high-energy cosmic neutrino flux in the presence of astrophysical background from nine years of IceCube data, Phys. Rev. D **98**, no. 6, 062003 (2018) doi:10.1103/PhysRevD.98.062003 [arXiv:1807.01820 [astro-ph.HE]].
[71] M. H. Reno, J. F. Krizmanic and T. M. Venters, Cosmic tau neutrino detection via Cherenkov signals from air showers from Earth-emerging taus, in preparation. [arXiv:1902.11287 [astro-ph.HE]].

[72] A. M. Dziewonski and D. L. Anderson, Preliminary reference Earth model, Physics of the Earth and Planetary Interiors **25**, 297 (1981).

[73] F. Halzen and D. Saltzberg, Tau-neutrino appearance with a 1000 megaparsec baseline, Phys. Rev. Lett. **81**, 4305 (1998) doi:10.1103/PhysRevLett.81.4305 [hep-ph/9804354].

[74] M. M. Block, L. Durand and P. Ha, Connection of the virtual $\gamma^* p$ cross section of ep deep inelastic scattering to real γp scattering, and the implications for νN and ep total cross sections, Phys. Rev. D **89**, no. 9, 094027 (2014) doi:10.1103/PhysRevD.89.094027 [arXiv:1404.4530 [hep-ph]].

[75] A. Albert *et al.* [ANTARES and IceCube and Pierre Auger and LIGO Scientific and Virgo Collaborations], Search for High-energy Neutrinos from Binary Neutron Star Merger GW170817 with ANTARES, IceCube, and the Pierre Auger Observatory, Astrophys. J. **850**, no. 2, L35 (2017) doi:10.3847/2041-8213/aa9aed [arXiv:1710.05839 [astro-ph.HE]].

[76] R Gandhi, C. Quigg, M.H. Reno, and I. Sarcevic, Neutrino interactions at ultrahigh-energies, Phys. Rev. D58, 093009 (1998), hep-ph/9807264",

[77] V. Berezinsky, E. Sabancilar and A. Vilenkin, Extremely high energy neutrinos from cosmic strings, Phys. Rev. D **84**, 085006 (2011) doi:10.1103/PhysRevD.84.085006 [arXiv:1108.2509 [astro-ph.CO]].

[78] V. A. Ryabov, V. A. Chechin, G. A. Gusev and K. T. Maung, Prospects for ultrahigh-energy particle observation based on the lunar orbital LORD space experiment, Adv. Space Res. **58**, 464 (2016). doi:10.1016/j.asr.2016.04.030

[79] P.W. Gorham, et al., (ANITA Collaboration) Constraints on the ultra-high energy cosmic neutrino flux from the fourth flight of ANITA, astro-ph.HE [arXiv:1902.04005]

[80] O. Scholten et al, Improved flux limits for neutrinos with energies above 10^{22} eV from observations with the Westerbork Synthesis Radio Telescope, Phys. Rev. Lett. 103: 191301 (2009) [arXiv:0910.4745 [astro-ph.HE]]

[81] J. P. Conlon and F. Quevedo, Astrophysical and cosmological implications of large volume string compactifications, JCAP **0708**, 019 (2007) doi:10.1088/1475-7516/2007/08/019 [arXiv:0705.3460 [hep-ph]].

[82] S. S. AbdusSalam, J. P. Conlon, F. Quevedo and K. Suruliz, Scanning the landscape of flux compactifications: Vacuum structure and soft supersymmetry breaking, JHEP **0712**, 036 (2007) doi:10.1088/1126-6708/2007/12/036 [arXiv:0709.0221 [hep-th]].

[83] R. Aloisio, S. Matarrese and A. V. Olinto, Super Heavy Dark Matter in light of BICEP2, Planck and Ultra High Energy Cosmic Rays Observations, JCAP **1508**, no. 08, 024 (2015) doi:10.1088/1475-7516/2015/08/024 [arXiv:1504.01319 [astro-ph.HE]].

[84] J. L. Christiansen, E. Albin, T. Fletcher, J. Goldman, I. P. W. Teng, M. Foley and G. F. Smoot, Search for cosmic strings in the COSMOS survey, Phys. Rev. D **83**, 122004 (2011) doi:10.1103/PhysRevD.83.122004 [arXiv:1008.0426 [astro-ph.CO]].

[85] R. van Haasteren *et al.*, Placing limits on the stochastic gravitational-wave background using European Pulsar Timing Array data, Mon. Not. Roy. Astron. Soc. **414**, no. 4, 3117 (2011) Erratum: [Mon. Not. Roy. Astron. Soc. **425**, no. 2, 1597 (2012)] doi:10.1111/j.1365-2966.2011.18613.x, 10.1111/j.1365-2966.2012.20916.x [arXiv:1103.0576 [astro-ph.CO]].

[86] T. Damour and A. Vilenkin, Gravitational radiation from cosmic (super)strings: Bursts, stochastic background, and observational windows, Phys. Rev. D **71**, 063510 (2005) doi:10.1103/PhysRevD.71.063510 [hep-th/0410222].

[87] S. Olmez, V. Mandic and X. Siemens, Gravitational-wave stochastic background from kinks and cusps on cosmic ctrings, Phys. Rev. D **81**, 104028 (2010) doi:10.1103/PhysRevD.81.104028

[arXiv:1004.0890 [astro-ph.CO]].
[88] L. A. Anchordoqui, H. Goldberg and T. J. Weiler, An Auger test of the Cen A model of highest energy cosmic rays, Phys. Rev. Lett. **87**, 081101 (2001) doi:10.1103/PhysRevLett.87.081101 [astro-ph/0103043].
[89] F. W. Stecker, Testing Lorentz Symmetry using High Energy Astrophysics Observations, Symmetry **9**, no. 10, 201 (2017) doi:10.3390/sym9100201 [arXiv:1708.05672 [astro-ph.HE]].
[90] P. W. Gorham *et al.*, Characteristics of four upward-pointing cosmic-ray-like events observed with ANITA, Phys. Rev. Lett. **117**, no. 7, 071101 (2016) doi:10.1103/PhysRevLett.117.071101 [arXiv:1603.05218 [astro-ph.HE]].
[91] P. W. Gorham *et al.* [ANITA Collaboration], Observation of an unusual upward-going cosmic-ray-like event in the third flight of ANITA, arXiv:1803.05088 [astro-ph.HE].
[92] A. Romero-Wolf *et al.*, A comprehensive analysis of anomalous ANITA events disfavors a diffuse tau-neutrino flux origin, arXiv:1811.07261 [astro-ph.HE].
[93] J. F. Cherry and I. M. Shoemaker, A sterile neutrino origin for the upward directed cosmic ray showers detected by ANITA, arXiv:1802.01611 [hep-ph].
[94] L. A. Anchordoqui, V. Barger, J. G. Learned, D. Marfatia and T. J. Weiler, Upgoing ANITA events as evidence of the CPT symmetric universe, LHEP **1**, no. 1, 13 (2018) doi:10.31526/LHEP.1.2018.03 [arXiv:1803.11554 [hep-ph]].
[95] G. y. Huang, Sterile neutrinos as a possible explanation for the upward air shower events at ANITA, Phys. Rev. D **98**, no. 4, 043019 (2018) doi:10.1103/PhysRevD.98.043019 [arXiv:1804.05362 [hep-ph]].
[96] E. Dudas, T. Gherghetta, K. Kaneta, Y. Mambrini and K. A. Olive, Gravitino decay in high scale supersymmetry with R -parity violation, Phys. Rev. D **98**, no. 1, 015030 (2018) doi:10.1103/PhysRevD.98.015030 [arXiv:1805.07342 [hep-ph]].
[97] A. Connolly, P. Allison and O. Banerjee, On ANITA's sensitivity to long-lived, charged massive particles, arXiv:1807.08892 [astro-ph.HE].
[98] D. B. Fox, S. Sigurdsson, S. Shandera, P. M??sz??ros, K. Murase, M. Mostaf?? and S. Coutu, The ANITA anomalous events as signatures of a beyond standard model particle, and supporting observations from IceCube, [arXiv:1809.09615 [astro-ph.HE]].
[99] J. H. Collins, P. S. Bhupal Dev and Y. Sui, R-parity violating supersymmetric explanation of the anomalous events at ANITA, arXiv:1810.08479 [hep-ph].
[100] B. Chauhan and S. Mohanty, A leptoquark resolution to flavor and ANITA anomalies, arXiv:1812.00919 [hep-ph].
[101] L. A. Anchordoqui and I. Antoniadis, Supersymmetric sphaleron configurations as the origin of the perplexing ANITA events, arXiv:1812.01520 [hep-ph].
[102] J. Adams *et al.* Space experiment TUS on board the Lomonosov satellite as pathfinder for JEM-EUSO Exp. Astron. **40**, 315 (2015).
[103] Aab et al., (The Pierre Auger Collaboration), A Three Year Sample of Almost 1600 Elves Recorded Above South America by the Pierre Auger Cosmic Ray Observatory, Submitted to Earth and Space Science (ESS) January 2019.
[104] R.K. Pachuri et al., Climate Change 2014, Synthesis Report. Contribution of working Groups I,II, and III to the Fifth Assessment Report of the Intergovernmental Panel on Climate Change, Geneva Switzerland: IPCC, 2014
[105] N.S Diffenbauch, M. Scherer, and R.J. Trapp, Robust increases in severe thunderstorm environments in response to greenhouse forcing, Proc. Of the National Academy of Sciences (USA), vol. 110 pp. 16361-6, Oct 2013.

[106] H. Brooks, Severe thunderstorms and climate change, Atmospheric Research, vol. 123, pp. 129-138, Apr 2013.
[107] J.H. Adams et al. (JEM-EUSO Coll.), JEM-EUSO: Meteor and nuclearite observations, Experimental Astronomy, Vol.40, 253-279 (2015).
[108] G. Abdellaoui et al. (JEM-EUSO Coll.), Meteor studies in the framework of the JEM-EUSO program, Planetary and Space Science, Vol. 143, 245-255 (2017).
[109] [3] A. De Rujula and S.L. Glashow, Nuclearites - a novel form of cosmic radiation, Nature, Vol.312, 734-737 (1984).
[110] G.E. Pavalas et al. (ANTARES Coll.), Search for massive exotic particles with the ANTARES neutrino telescope, Proceedings 23rd ECRS, Moscow, 543 (2012).
[111] P.B. Price, Limits on contribution of cosmic nuclearites to galactic dark matter, Physical Review D, Vol. 38, 3813-3814 (1988).
[112] F. W. Stecker, J. F. Krizmanic, L. M. Barbier, E. Loh, J. W. Mitchell, P. Sokolsky and R. E. Streitmatter, Observing the ultrahigh-energy universe with OWL eyes, Nucl. Phys. Proc. Suppl. **136C**, 433 (2004) doi:10.1016/j.nuclphysbps.2004.10.027 [astro-ph/0408162].
[113] A. Neronov, D. V. Semikoz, L. A. Anchordoqui, J. Adams and A. V. Olinto, Sensitivity of a proposed space-based Cherenkov astrophysical-neutrino telescope, Phys. Rev. D **95**, no. 2, 023004 (2017) doi:10.1103/PhysRevD.95.023004 [arXiv:1606.03629 [astro-ph.IM]].
[114] L. Wiencke *et al.* [JEM-EUSO Collaboration], EUSO-SPB1 mission and science, PoS ICRC **2017**, 1097 (2018). doi:10.22323/1.301.1097
[115] J. H. Adams *et al.*, White paper on EUSO-SPB2, arXiv:1703.04513 [astro-ph.HE].
[116] J. H. Adams et al. (JEM-EUSO Collaboration), Calibration aspects of the JEM-EUSO mission, Experimental Astronomy, 40(1):91116, Nov 2015, URL https://doi.org/10.1007/s10686-015-9453-2.
[117] J. H. Adams et al. (JEM-EUSO Collaboration), The infrared camera onboard JEMEUSO, Experimental Astronomy, 40(1):6189, Nov 2015, URL https://doi.org/10.1007/s10686-014-9402-5.
[118] L. Allen et al. (JEM-EUSO Collaboration), UCIRC: Infrared Cloud Monitor for EUSO-SPBin Proc. 35th ICRC, PoS, ICRC2017:436, 2018.
[119] A. Anzalone, M. E. Bertaina, S. Briz, C. Cassardo, R. Cremonini, A. J. de Castro, S. Ferrarese, F. Isgr, F. Lopez, I. Tabone, Methods to Retrieve the Cloud-Top Height in the Frame of the JEM-EUSO Mission, IEEE Transactions on Geoscience and Remote Sensing, Vol. 57, pag. 304-318 (2019).
[120] J.A. Banik, AFRL, Realizing Large Structures in Space, National Academy of Engineering, 2015 US Frontiers of Engineering, 9-11 September 2015 Irvine, California
[121] M. Ackermann et al., Astrophysics Uniquely Enabled by Observations of High-Energy Cosmic Neutrinos, Astro2020 Science White Paper (2019)
[122] M. Ackermann et al., Fundamental Physics with High-Energy Cosmic Neutrinos Astro2020 Science White Paper (2019).